

A Picture of Solar-Sail Heteroclinic Enhanced Connections between Lissajous Libration Point Orbits

Xun Duan *

National Key Laboratory of Aerospace Flight Dynamics, Northwestern Polytechnical University & Universitat de Barcelona & Universitat Politècnica de Catalunya

Gerard Gómez †

IEEC & Universitat de Barcelona

Josep J. Masdemont‡

IEEC & Universitat Politècnica de Catalunya

Xiaokui Yue§

National Key Laboratory of Aerospace Flight Dynamics, Northwestern Polytechnical University

July 15, 2019

Abstract

The dynamics of solar-sail maneuvers is conceptually different from classical control maneuvers where one considers impulsive changes in the velocity of a spacecraft. Solar-sail orbits are continuous in both position and velocity in a varying vectorfield, opening the possibility of the existence of heteroclinic connections by means of artificially changing the vectorfield with a sail maneuver. This paper investigates solar-sail assisted maneuvers to obtain families of artificial heteroclinic connections joining Lissajous libration point orbits. The study is based on a careful analysis of the geometry of the phase space of the linearized equations around the equilibrium points, the dynamical identification of the main parameters and the representation of the solutions in the action-angle variables. We identify the main dynamical properties of the connecting families presenting systematic new options for the mission analysis in the libration point regime using this technology, including a methodology to approach the classical problem of exclusion zone avoidance.

1 Introduction

Homoclinic and heteroclinic orbits have a key role when analyzing the structural dynamics of a system and, in particular, for designing transfer trajectories in space missions [1, 2, 3, 4, 5]. They are seen as "zero cost" transfer

*Ph.D. Candidate. School of Astronautics, Road West 127, Xi'an 710072, China. npudian@mail.nwpu.edu.cn.

†Professor. UB-Departament de Matemàtiques i Informàtica, Gran Via de les Corts Catalanes 585, 08007 Barcelona. gerard@maia.ub.es.

‡Professor. UPC-Departament de Matemàtiques, Diagonal 647, 08028 Barcelona. josep.masdemont@upc.edu.

§Professor. School of Astronautics, Road West 127, Xi'an 710072, China. xkyue@nwpu.edu.cn.

orbits, since in theory, no maneuvers are needed to transfer between the α and ω limits that they connect. From another side, nowadays there exist an increasing interest for missions involving spacecraft with large solar sails. Solar sails can be seen as a spacecraft propulsion device where the momentum of the Solar Radiation Pressure (SRP) emitted by the Sun accelerates the satellite [6]. In particular, attending libration point orbits, a number of technological applications have been considered, involving for instance: polar coverage [7, 8, 9], the Earth-Moon system [10, 11], hybrid techniques [12, 13], feedback control possibilities [14] and the exploration of binary asteroids [15].

Solar-sail maneuvers are performed by changing the spacecraft sail’s attitude with respect to the Sun or by changing the sail reflective properties. Opposite to the classical maneuvers, that involve an impulsive change of velocity by means of a propulsion device, solar sail maneuvers imply a step change in the acceleration. From a dynamic system point of view, the vectorfield changes as a result of the maneuver, but the state of the spacecraft remains the same. It is in this context that one can see solar sail maneuvers as “zero cost” maneuvers, and when a transfer between to different orbits is performed using this technique, we talk about an heteroclinic enhanced connection, since the trajectory is continuous in both position and velocity, inside a changing vectorfield.

As it is general for the analysis of libration point orbits, in our work we consider the Sun-Earth Circular Restricted Three-Body Problem (CR3BP). The CR3BP model has five equilibrium points (L_i , $i = 1 \dots 5$), all of them on the ecliptic plane (this is, with coordinate $z = 0$) [16]. When the SRP acceleration is added to this model, the equilibrium points subsist but their position varies according to the sail’s attitude with respect to the Sun [6, 17]. We use the notation SL_i to differentiate them from the classical L_i ones of the CR3BP. Libration point orbits (LPOs) are periodic or quasi-periodic orbits around the equilibrium points, such as planar and vertical Lyapunov periodic orbits, halo periodic orbits, and Lissajous quasi-periodic orbits [18, 19]. Similar to the equilibrium points, LPO orbits undergo under displacements in the CR3BP-SRP model, as it has been carefully studied in [20, 21, 22].

LPO are very useful for Sun and space observations including a rich variety of sizes and shapes (see[18] and references therein). Even that, in the same basis, the present analysis could be also made for LPO about SL_1 , we have considered Lissajous orbits around collinear libration points SL_2 , that can be more popular in terms of the number of potential missions, and in view of the current Chinese Change’E series [23, 24, 25]. Moreover, transfers between Lissajous orbits are advantageous for reaching higher or lower amplitude sizes, for avoiding escape from the nominal orbit (due to their inherent instability), for avoiding forbidden zones, such as the ones related to eclipse avoidance for missions around L_1 , or for avoiding the Earth shadow cone for missions around the L_2 point[26].

The SRP acceleration model considered in this paper depends on three parameters: the lightness parameter, which is a function of the spacecraft’s reflectivity and area-to-mass ratio [5], and the normal unitary vector to the sail determining its attitude and it is represented as a function of the so called cone and clock angles α and δ . As previously stated, the maneuvers under consideration are performed by means of a change in the solar sail reflectivity or by re-orienting the sail. Our goal is to do a general study of all possible transfers between Lissajous orbits changing these three parameters. The approach we follow is geometrical [5] and is mainly based in the analysis of the linearized equations of motion around the equilibrium points [27]. Taking into account that with an SRP maneuver the location of the artificial libration point changes, using a reference system always centered on the nominal current SL_2 , a SRP maneuver is seen as a jump in the relative position instead of in velocity. The paper uses this fact to systematically analyze the impact of a maneuver on a satellite on a libration point trajectory. Considering maneuvers that do not introduce unstable components in the modes of motion (that would produce divergence from the libration zone) one obtains the heteroclinic enhanced connections between Lissajous orbits.

The paper, is organized as follows: Section 2 presents the equations of motion and the families of equilibrium points of the CR3BP-SRP for different values of the sail parameters. The solutions of the linearized CR3BP-SRP model, around the collinear equilibrium points, are computed in Section 3. These solutions are used in Section 4 to determine the heteroclinics using SRP maneuvers. Finally, Section 5 accounts for a particular transfer strategy to avoid the exclusion zones associated to libration point missions. The paper ends with some conclusions.

2 Equations of Motion

We consider the motion of an infinitesimal mass body (spacecraft) provided with a solar sail under the gravitational attraction of two point masses, m_1 and m_2 , such as the Sun and the Earth. The dynamical model is the three-dimensional circular restricted three-body problem (CR3BP) including solar radiation pressure (SRP); from now on

the CR3BP-SRP model.

As is usual in the CR3BP (see [16]) we take a synodic reference system, (X, Y, Z) , with the origin at the center of mass of the two primaries, and normalized units of mass, length and time. So μ denotes the mass of the Earth located at $(\mu-1,0,0)$, and $1-\mu$ the mass of the Sun located at $(\mu,0,0)$ [28].

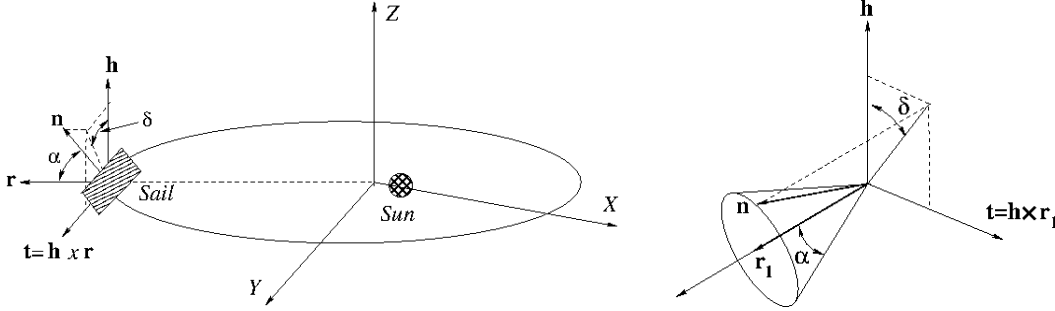


Figure 1: Schematic representation of the sail orientation angles α and δ .

The solar sail orientation is defined by the unitary normal vector to its surface, \mathbf{n} , which depends on two angles: the *cone angle* α , and the *clock angle* δ . For their definition we consider a reference frame, $\mathbf{r}_1, \mathbf{h}, \mathbf{t}$, centered at the spacecraft, such that: \mathbf{r}_1 is in the Sun-spacecraft direction, \mathbf{h} is perpendicular to the orbital plane, so parallel to Z , and \mathbf{t} completes an orthogonal positive oriented frame. Then, α is the angle between \mathbf{n} and \mathbf{r}_1 that measures the elongation of \mathbf{n} with respect to the Sun, and δ is the angle between the \mathbf{h} axis and the projection of \mathbf{n} onto the (\mathbf{h}, \mathbf{t}) plane (see Fig. 1). The range of α is $[-\pi/2, \pi/2]$, since it is not feasible to produce acceleration towards the Sun, and the one of δ is $[0, 2\pi]$.

The equations of motion of the model are,

$$\begin{cases} \ddot{X} - 2\dot{Y} &= \Omega_X + a_X^s, \\ \ddot{Y} + 2\dot{X} &= \Omega_Y + a_Y^s, \\ \ddot{Z} &= \Omega_Z + a_Z^s, \end{cases} \quad (1)$$

being Ω_X, Ω_Y and Ω_Z the partial derivatives of $\Omega(X, Y, Z)$,

$$\Omega(X, Y, Z) = \frac{1}{2}(X^2 + Y^2) + \frac{1-\mu}{r_1} + \frac{\mu}{r_2} + \frac{1}{2}\mu(1-\mu),$$

where r_1 and r_2 are the distances from the solar sail to the Sun and to the Earth, respectively, this is,

$$r_1^2 = (X - \mu)^2 + Y^2 + Z^2, \quad r_2^2 = (X - \mu + 1)^2 + Y^2 + Z^2.$$

Finally, a_X^s, a_Y^s, a_Z^s are the three components of the SRP acceleration \mathbf{a}^s which, according to [6], is given by:

$$\mathbf{a}^s = \beta \frac{1-\mu}{r_1^2} \cos^2 \alpha \mathbf{n},$$

where $\beta \in [0, 1]$ is the lightness number, related to the reflectivity of the sail. Therefore, if $\mathbf{z} = (0, 0, 1)$,

$$\begin{aligned} a_X^s &= \frac{\beta(1-\mu)(X-\mu)}{|\mathbf{r}_1|^3} \cos^3 \alpha - \frac{\beta(1-\mu)(X-\mu)Z}{|\mathbf{r}_1|^2 |(\mathbf{r}_1 \times \mathbf{z}) \times \mathbf{r}_1|} \cos^2 \alpha \sin \alpha \cos \delta + \frac{\beta(1-\mu)Y}{|\mathbf{r}_1|^2 |(\mathbf{r}_1 \times \mathbf{z})|} \cos^2 \alpha \sin \alpha \sin \delta, \\ a_Y^s &= \frac{\beta(1-\mu)Y}{|\mathbf{r}_1|^3} \cos^3 \alpha - \frac{\beta(1-\mu)YZ}{|\mathbf{r}_1|^2 |(\mathbf{r}_1 \times \mathbf{z}) \times \mathbf{r}_1|} \cos^2 \alpha \sin \alpha \cos \delta - \frac{\beta(1-\mu)(X-\mu)}{|\mathbf{r}_1|^2 |(\mathbf{r}_1 \times \mathbf{z})|} \cos^2 \alpha \sin \alpha \sin \delta, \\ a_Z^s &= \frac{\beta(1-\mu)Z}{|\mathbf{r}_1|^3} \cos^3 \alpha - \frac{\beta(1-\mu)(Y^2 + (X-\mu)^2)}{|\mathbf{r}_1|^2 |(\mathbf{r}_1 \times \mathbf{z}) \times \mathbf{r}_1|} \cos^2 \alpha \sin \alpha \cos \delta. \end{aligned}$$

When the reflectivity parameter β is zero, or when $\alpha = \pm\pi/2$, we recover the CR3BP equations. Besides, taking the clock angle $\delta = \pi/2$, then \mathbf{n} is the plane expanded by $\mathbf{r}_1 \times \mathbf{h}$, and \mathbf{r}_1 and it does not exist any SRP acceleration in the direction orthogonal to \mathbf{h} .

2.1 Equilibrium Points of the CR3BP-SRP Model

The equilibrium points of the CR3BP-SRP model are the solutions of the system,

$$\Omega_X + a_X^s = 0, \quad \Omega_Y + a_Y^s = 0, \quad \Omega_Z + a_Z^s = 0.$$

It is well known that the CR3BP ($a_X^s = a_Y^s = a_Z^s = 0$) has five equilibrium points, usually denoted by L_1, L_2, \dots, L_5 . When further considering SRP the new points will be denoted by SL_1, SL_2, \dots, SL_5 . We are interested in the two ones that are close to the Earth, this is SL_1 and SL_2 , and in their location when the cone angle α , the clock angle δ , and the lightness number β vary. This problem has already been considered by different authors, including [6, 21, 17, 5].

Let us consider the main relevant cases:

- When $\alpha = \pm\pi/2$ then $\hat{\mathbf{n}} \perp \hat{\mathbf{r}}$, so $\hat{\mathbf{a}}^s = \mathbf{0}$ and, since the model coincides with the CR3BP: $SL_i = L_i$ for $i = 1, \dots, 5$.
- When $\alpha = 0$, then the plane of the solar sail is perpendicular to $\hat{\mathbf{r}}$. In this case the force due to the SRP is aligned with the gravitational attraction of the Sun, so the model can be seen as the usual CR3BP with the mass of the Sun, $1 - \mu$, decreased. The position of SL_1 and SL_2 moves towards the Sun as the value of β increases.
- In the third case α can take any value, and δ can take any of the following values: $\pm\pi/2, \pi$, or 0 .

In this case there is an extra force in the X - Y plane that displaces (left/right) the equilibrium point. If $\delta = 0$ or $\delta = \pi$, the extra force will be in the vertical direction and will displace the equilibrium above/below the X - Y plane.

When α and δ vary in $(-\pi/2, \pi/2)$ and $(0, 2\pi)$, respectively, the equilibrium points $SL_1(\alpha, \delta)$ and $SL_2(\alpha, \delta)$ define a 2D surface homeomorphic to a sphere; each equilibrium point on the sphere corresponds to a given sail orientation. As β varies between 0 and 1 the two surfaces of equilibrium points $SL_1(\alpha, \delta)$ and $SL_2(\alpha, \delta)$ also change. The evolution with β is shown in Figs 2 and 3. In the $SL_1(\alpha, \delta)$ case, for small values of β there is only one sphere of equilibrium points, if $\beta \in (0.03, 0.07)$ then $SL_1(\alpha, \delta)$ has two components, and for $\beta > 0.07$ one of the two components (the one in blue in the plots) merges with the SL families associated to L_3, L_4 and L_5 , which are not considered in this paper.

3 The analytical linear CR3BP-SRP model and its solution

From now on, we focus our attention on the motion in the vicinity of SL_2 (the study around SL_1 is similar). For given values of α, δ and on β , let $(\gamma_1, \gamma_2, \gamma_3)$ be the position of SL_2 in the CR3BP reference frame and units. Following [5], we perform a change of scale, and set the origin of coordinates at the equilibrium point by means of the translation,

$$\begin{cases} X &= \gamma x + \gamma_1, \\ Y &= \gamma y + \gamma_2, \\ Z &= \gamma z + \gamma_3, \end{cases}$$

where γ is a scaling factor chosen in order to normalize the Earth-equilibrium point distance. In our case, we have taken $\gamma = 0.01$, since this value is very close to the Earth- L_2 distance in the CR3BP. Therefore, in the new coordinates, the adimensional distance unit will be, approximately, 1.5×10^6 km.

Applying the above change of coordinates to the CR3BP-SRP equations we get,

$$\begin{cases} \ddot{x} - 2\dot{y} &= \frac{1}{\gamma^2}\Omega_x + \frac{1}{\gamma}a_x^s, \\ \ddot{y} + 2\dot{x} &= \frac{1}{\gamma^2}\Omega_y + \frac{1}{\gamma}a_y^s, \\ \ddot{z} &= \frac{1}{\gamma^2}\Omega_z + \frac{1}{\gamma}a_z^s. \end{cases}$$

and the linearized equations of motion at the equilibrium point become,

$$\begin{cases} \ddot{x} - 2\dot{y} &= a_1x + a_2y + a_3z, \\ \ddot{y} + 2\dot{x} &= b_1x + b_2y + b_3z, \\ \ddot{z} &= c_1x + c_2y + c_3z, \end{cases} \quad (2)$$

where the coefficients a_i, b_i and c_i , that depend on $\mu, \alpha, \delta, \beta, \gamma_1, \gamma_2, \gamma_3$, and γ are explicitly given in Appendix A.

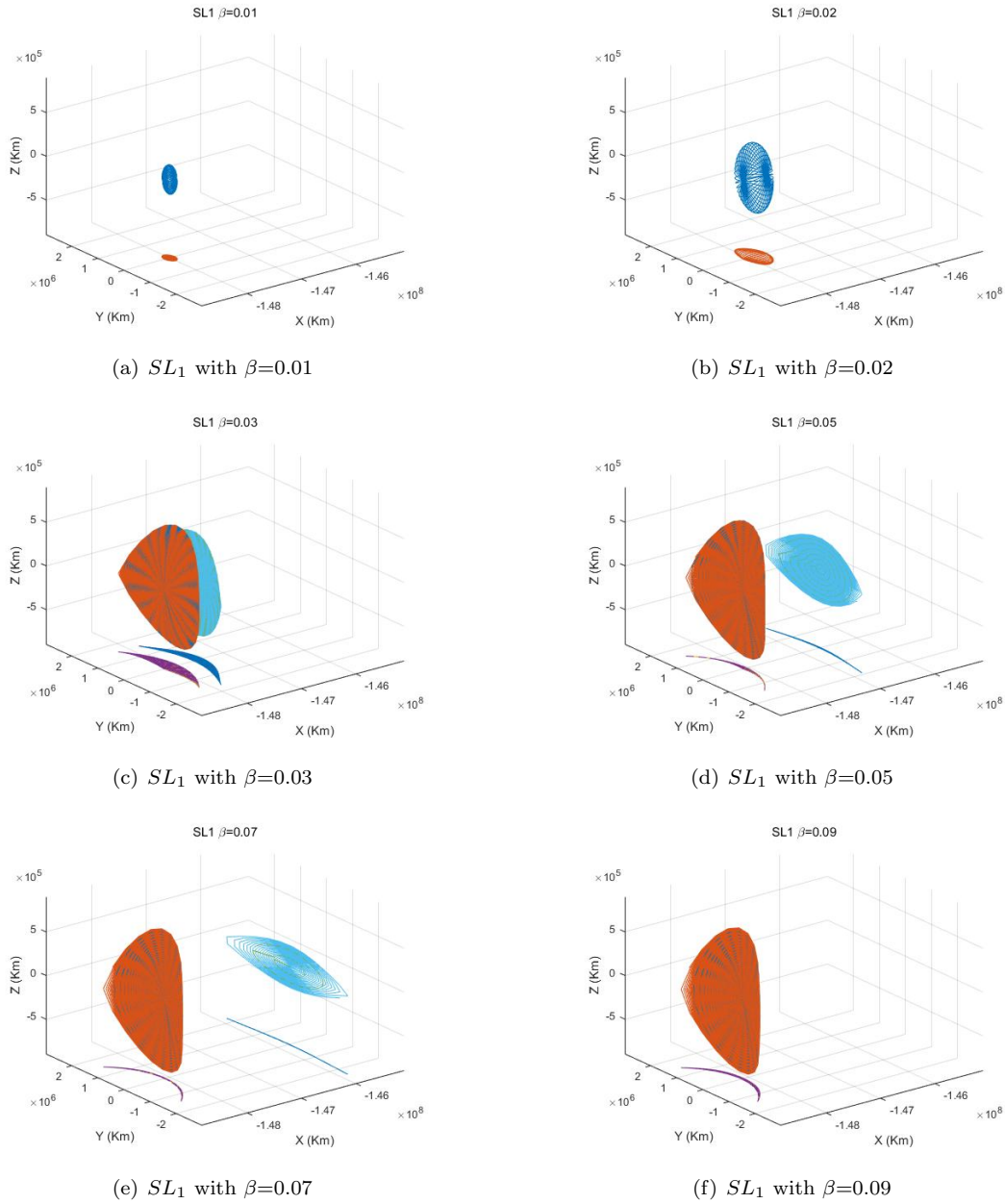


Figure 2: $SL_1(\alpha, \delta)$ equilibrium points families for different values of β . In each plot $\alpha \in (-\pi/2, \pi/2)$, and $\delta \in (0, 2\pi)$.

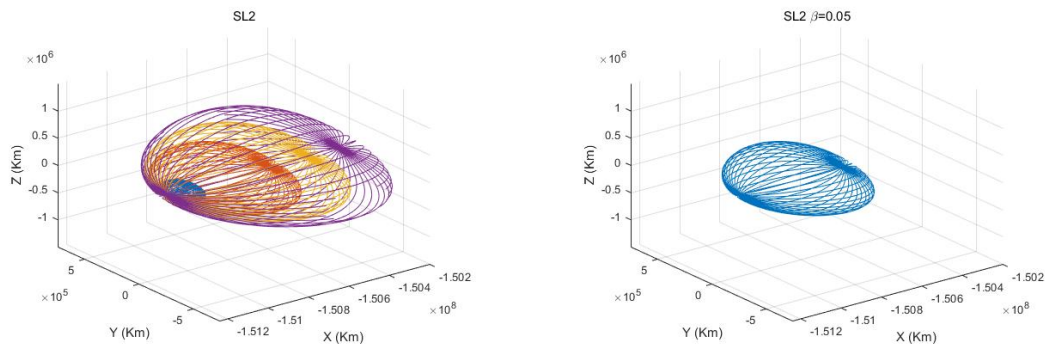


Figure 3: $SL_2(\alpha, \delta)$ equilibrium points families. In the left plot β takes four different values: 0.01, 0.05, 0.09, and 0.13. In the right plot $\beta = 0.05$.

3.1 Analytical solution of the linearized equations

We look for solutions of the linear system (1) with one of the following two patterns, that will be respectively associated to planar and vertical modes of motion,

$$\begin{aligned} \text{Case 1:} \quad & x(t) = e^{\lambda t}, \quad y(t) = ke^{\lambda t}, \quad z(t) = \bar{k}e^{\lambda t}, \\ \text{Case 2:} \quad & x(t) = \bar{k}e^{\lambda t}, \quad y(t) = ke^{\lambda t}, \quad z(t) = e^{\lambda t}, \end{aligned} \tag{3}$$

where, in both cases, the parameters k , \bar{k} , and the exponent λ are, in general, complex numbers to be determined independently for each case.

Inserting (3) into the differential equations (2) we get the following two systems of equations for the parameters,

$$\text{Case 1:} \quad \begin{cases} \lambda^2 - 2k\lambda = a_1 + a_2k + a_3\bar{k}, \\ k\lambda^2 + 2\bar{k}\lambda = b_1 + b_2k + b_3\bar{k}, \\ \bar{k}\lambda^2 = c_1 + c_2k + c_3\bar{k}, \end{cases} \quad \text{Case 2:} \quad \begin{cases} \bar{k}\lambda^2 - 2k\lambda = a_1\bar{k} + a_2k + a_3, \\ k\lambda^2 + 2\bar{k}\lambda = b_1\bar{k} + b_2k + b_3, \\ \lambda^2 = c_1\bar{k} + c_2k + c_3. \end{cases}$$

In both cases the exponent λ must fulfill the following 6-th degree polynomial equation,

$$\begin{aligned} \lambda^6 - (a_1 + b_2 + c_3 - 4)\lambda^4 + (2a_2 - 2b_1)\lambda^3 - (4c_3 - a_1b_2 + a_2b_1 - a_1c_3 + a_3c_1 - b_2c_3 + b_3c_2)\lambda^2 \\ - 2(a_2c_3 - a_3c_2 - b_1c_3 + b_3c_1)\lambda - a_3b_1c_2 - a_2b_3c_1 - a_1b_2c_3 + a_3b_2c_1 + a_2b_1c_3 + a_1b_3c_2 = 0. \end{aligned} \tag{4}$$

For the equilibrium points SL_1 and SL_2 , two roots of this polynomial, $\lambda_{1,2}$ ($\lambda_1 > 0$, $\lambda_2 < 0$), are always real, and the remaining ones are two complex conjugate pairs: $\lambda_{3,4} = \eta_1 \pm \omega_1 i$ and $\lambda_{5,6} = \eta_2 \pm \omega_2 i$. In general, $\lambda_1 \simeq -\lambda_2$, and the equality only holds when $\alpha = 0$.

For a given value of λ , solution of (4), the associated values of k and \bar{k} depend on the case under consideration.

In Case 1 we get,

$$k = \frac{\lambda^4 - (c_3 + a_1)\lambda^2 + a_1c_3 - a_3c_1}{2\lambda^3 + a_2\lambda^2 - 2c_3\lambda - a_2c_3 + a_3c_2}, \tag{5}$$

$$\bar{k} = \frac{c_2\lambda^4 + 2c_1\lambda^3 + (a_2c_1 - c_2c_3 - a_1c_2)\lambda^2 - 2c_1c_3\lambda + a_1c_2c_3 - a_2c_1c_3}{2\lambda^5 + a_2\lambda^4 - 4c_3\lambda^3 + (a_3c_2 - 2a_2c_3)\lambda^2 + 2c_3^2\lambda + a_2c_3^2 - a_3c_2c_3}, \tag{6}$$

while in Case 2 the values of k and \bar{k} are,

$$k = \frac{\lambda^4 - (c_3 + a_1)\lambda^2 + a_1c_3 - a_3c_1}{c_2\lambda^2 + 2c_1\lambda - a_1c_2 + a_2c_1}, \quad \bar{k} = \frac{2\lambda^3 + a_2\lambda^2 - 2c_3\lambda - a_2c_3 + a_3c_2}{c_2\lambda^2 + 2c_1\lambda a_1c_2 + a_2c_1}. \tag{7}$$

From the expressions given in Appendix A, it follows that if $\gamma_3 = 0$ then $C_1 = C_2 = C_3 = 0$; furthermore, according to the values of c_1 and c_2 :

$$\begin{aligned} c_1 &= \frac{1 - \mu}{\gamma^3} \frac{3A_1C_1}{D_1^5} + \frac{\mu}{\gamma^3} \frac{3A_2C_2}{D_2^5} - \frac{\beta(1 - \mu) \cos^2 \alpha}{\gamma^3 D_1^3 D_3} \left(\frac{3A_1C_1D_3}{D_1^2} \cos \alpha - (E_3D_3^2 - 2)A_1 \sin \alpha \cos \delta \right), \\ c_2 &= \frac{1 - \mu}{\gamma^3} \frac{3C_1B_1}{D_1^5} + \frac{\mu}{\gamma^3} \frac{3B_2C_2}{D_2^5} - \frac{\beta(1 - \mu) \cos^2 \alpha}{\gamma^3 D_1^3 D_3} \left(\frac{3B_1C_1D_3}{D_1^2} \cos \alpha - (E_3D_3^2 - 2)B_1 \sin \alpha \cos \delta \right), \end{aligned}$$

it follows that if $\alpha = 0$ or $\alpha = \pi$, and $\delta = \pi/2$, then $c_1 = c_2 = 0$, so the the expressions (7) of k and \bar{k} in Case 2 become singular. In other to avoid this situation, we can write k and \bar{k} in terms of a_i and b_i as,

$$\begin{aligned} k &= \frac{b_3\lambda^2 - 2a_3\lambda - a_1b_3 + a_3b_1}{\lambda^4 - (a_1 + b_2 - 4)\lambda^2 + (2a_2 - 2b_1)\lambda + a_1b_2 - a_2b_1}, \\ \bar{k} &= \frac{a_3\lambda^2 + 2b_3\lambda + a_2b_3 - a_3b_2}{\lambda^4 - (a_1 + b_2 - 4)\lambda^2 + (2a_2 - 2b_1)\lambda + a_1b_2 - a_2b_1}, \end{aligned}$$

which are not singular for the above values of the parameters. Something similar happens in Case 1, in this case the singularity disappears using the following expressions for k and \bar{k} ,

$$k = \frac{-2\lambda^3 + b_3\lambda^2 + 2a_1\lambda - a_1b_3 + a_3b_1}{(a_3 - 4)\lambda^2 + 2(b_3 - a_2)\lambda + a_2b_3 - a_3b_2}, \quad \bar{k} = \frac{\lambda^4 - (a_1 + b_2)\lambda^2 - 2b_1\lambda + a_1b_2 - b_1a_2}{(a_3 - 4)\lambda^2 + 2(b_3 - a_2)\lambda + a_2b_3 - a_3b_2}.$$

In Case 1, the solution of the differential equations (2) associated to the planar mode can be written as:

$$\begin{aligned} x(t) &= A_1e^{\lambda_1 t} + A_2e^{\lambda_2 t} + A_3e^{\eta_1 t} \cos \omega_1 t + A_4e^{\eta_1 t} \sin \omega_1 t, \\ y(t) &= A_1k_1e^{\lambda_1 t} + A_2k_2e^{\lambda_2 t} + A_3e^{\eta_1 t}(k_3 \cos \omega_1 t + k_4 \sin \omega_1 t) + A_4e^{\eta_1 t}(k_3 \sin \omega_1 t - k_4 \cos \omega_1 t), \\ z(t) &= A_1\bar{k}_1e^{\lambda_1 t} + A_2\bar{k}_2e^{\lambda_2 t} + A_3e^{\eta_1 t}(\bar{k}_3 \cos \omega_1 t + \bar{k}_4 \sin \omega_1 t) + A_4e^{\eta_1 t}(\bar{k}_3 \sin \omega_1 t - \bar{k}_4 \cos \omega_1 t), \end{aligned}$$

and in Case 2, associated to the vertical mode, as:

$$\begin{aligned} x(t) &= A_5e^{\eta_2 t}(\bar{k}_5 \cos \omega_2 t + \bar{k}_6 \sin \omega_2 t) + A_6e^{\eta_2 t}(\bar{k}_5 \sin \omega_2 t - \bar{k}_6 \cos \omega_2 t), \\ y(t) &= A_5e^{\eta_2 t}(k_5 \cos \omega_2 t + k_6 \sin \omega_2 t) + A_6e^{\eta_2 t}(k_5 \sin \omega_2 t - k_6 \cos \omega_2 t), \\ z(t) &= A_5e^{\eta_2 t} \cos \omega_2 t + A_6e^{\eta_2 t} \sin \omega_2 t. \end{aligned}$$

So, in general, the final form of the solution (2) containing all modes becomes:

$$\begin{aligned} x(t) &= A_1e^{\lambda_1 t} + A_2e^{\lambda_2 t} + A_3e^{\eta_1 t} \cos \omega_1 t + A_4e^{\eta_1 t} \sin \omega_1 t \\ &\quad + A_5e^{\eta_2 t}(\bar{k}_5 \cos \omega_2 t + \bar{k}_6 \sin \omega_2 t) + A_6e^{\eta_2 t}(\bar{k}_5 \sin \omega_2 t - \bar{k}_6 \cos \omega_2 t), \\ y(t) &= A_1k_1e^{\lambda_1 t} + A_2k_2e^{\lambda_2 t} + A_3e^{\eta_1 t}(k_3 \cos \omega_1 t + k_4 \sin \omega_1 t) + A_4e^{\eta_1 t}(k_3 \sin \omega_1 t - k_4 \cos \omega_1 t) \\ &\quad + A_5e^{\eta_2 t}(k_5 \cos \omega_2 t + k_6 \sin \omega_2 t) + A_6e^{\eta_2 t}(k_5 \sin \omega_2 t - k_6 \cos \omega_2 t), \\ z(t) &= A_1\bar{k}_1e^{\lambda_1 t} + A_2\bar{k}_2e^{\lambda_2 t} + A_3e^{\eta_1 t}(\bar{k}_3 \cos \omega_1 t + \bar{k}_4 \sin \omega_1 t) + A_4e^{\eta_1 t}(\bar{k}_3 \sin \omega_1 t - \bar{k}_4 \cos \omega_1 t) \\ &\quad + A_5e^{\eta_2 t} \cos \omega_2 t + A_6e^{\eta_2 t} \sin \omega_2 t. \end{aligned} \tag{8}$$

In these equations A_1, \dots, A_6 are arbitrary parameters, $\lambda_{1,2}$ are the real roots of (4), ($\lambda_1 > 0, \lambda_2 < 0$), and $\lambda_{3,4} = \eta_1 \pm \omega_1 i$ and $\lambda_{5,6} = \eta_2 \pm \omega_2 i$ are the two complex conjugate pairs. The eigenvalues $\lambda_{3,4}$ are the ones associated to the planar oscillations of the solutions, and $\lambda_{5,6}$ are the ones associated to the vertical ones. The values of k_i and \bar{k}_i , for $i = 1, \dots, 6$, are given in Appendix B.

An important property of the formulation chosen in (8) is that it gives a continuous global representation when crossing bifurcations varying the values α, δ, β and changing the type of equilibrium point associated. To have a general idea of the magnitude of the eigenvalues, Table 1 shows some values of $\lambda_{1,2}, \eta_{1,2}, \omega_{1,2}$ depending on α and δ for $\beta = 0.02$. From the first two lines, we see that if $\alpha = 0$, the eigenvalues do not change no matter what value of δ . Lines 3 to 9 show how the variation of eigenvalues when $\delta = \pi/2$ and the value of α changes. Lines 10 to 20 show the behavior of the roots when $\alpha = \pi/6$, and the value of δ varies.

The expression (8) can be also written in matrix form as,

$$[x(t), y(t), z(t), \dot{x}(t), \dot{y}(t), \dot{z}(t)]^T = H(t) [A_1, A_2, A_3, A_4, A_5, A_6]^T, \tag{9}$$

where the components of the matrix H are given in Appendix C. Inverting the above system we get,

$$[A_1, A_2, A_3, A_4, A_5, A_6]^T = H^{-1}(t) [x(t), y(t), z(t), \dot{x}(t), \dot{y}(t), \dot{z}(t)]^T, \tag{10}$$

that, for $t = 0$ gives the values of the amplitudes as a function of the initial conditions,

$$[A_1, A_2, A_3, A_4, A_5, A_6]^T = H^{-1}(0) [x_0, y_0, z_0, \dot{x}_0, \dot{y}_0, \dot{z}_0]^T. \tag{11}$$

Unfortunately, it is not possible to write short expressions for the components of the matrix $H^{-1}(t)$.

It is also convenient to write the oscillatory solutions (8) of the differential equations (2) using amplitudes and associated phases. Defining the unstable and stable amplitudes, A_u and A_s , and the planar (in-plane) and vertical (out-of-plane) amplitudes, $A_x = \sqrt{A_3^2 + A_4^2}$ and $A_z = \sqrt{A_5^2 + A_6^2}$, respectively, by means of the relations,

$$A_1 = A_u, \quad A_2 = A_s, \quad A_3 = A_x \cos \phi_1, \quad A_4 = -A_x \sin \phi_1, \quad A_5 = A_z \cos \phi_2, \quad A_6 = -A_z \sin \phi_2, \tag{12}$$

Table 1: Some relevant example values of $\lambda_{1,2}$, $\eta_{1,2}$, $\omega_{1,2}$ depending on α and δ for a given $\beta = 0.02$.

No.	α	δ	λ_1	λ_2	η_1	ω_1	η_2	ω_2
1	0	$\pi/2$	3.30475	-3.30475	0	2.57190	0	2.51131
2	0	$\pi/4$	3.30475	-3.30475	0	2.57190	0	2.51131
3	$\pi/6$	$\pi/2$	3.00566	-3.00466	-0.00050	2.37048	0	2.32633
4	$\pi/4$	$\pi/2$	2.75492	-2.75382	-0.00055	2.21122	0	2.16727
5	$\pi/3$	$\pi/2$	2.57546	-2.57471	-0.00038	2.10685	0	2.04750
6	$-\pi/6$	$\pi/2$	3.00466	-3.00566	0.00050	2.37048	0	2.32633
7	$-\pi/4$	$\pi/2$	2.75382	-2.75492	0.00055	2.21122	0	2.16727
8	$-\pi/3$	$\pi/2$	2.57470	-2.57546	0.00038	2.10685	0	2.04750
9	$\pm \pi/2$	$\pi/2$	2.48432	-2.48432	0	2.05701	0	1.98508
10	$\pi/6$	0	3.01329	-3.01329	0	2.48569	0	2.21387
11	$\pi/6$	$\pi/6$	3.01150	-3.01100	-0.00014	2.46770	-0.00011	2.23117
12	$\pi/6$	$\pi/3$	3.00762	-3.00676	-0.00027	2.41942	-0.00016	2.27808
13	$\pi/6$	$\pi/2$	3.00566	-3.00466	-0.00050	2.37048	0	2.32633
14	$\pi/6$	$2\pi/3$	3.00762	-3.00676	-0.00027	2.41942	-0.00016	2.27808
15	$\pi/6$	$5\pi/6$	3.01150	-3.01100	-0.00014	2.46770	-0.00011	2.23117
16	$\pi/6$	π	3.01329	-3.01329	0	2.48569	0	2.21387
17	$\pi/6$	$7\pi/6$	3.01100	-3.01150	0.00014	2.46770	0.00011	2.23117
18	$\pi/6$	$2\pi/3$	3.00676	-3.00762	0.00027	2.41942	0.00016	2.27808
19	$\pi/6$	$3\pi/2$	3.00466	-3.00566	0.00050	2.37048	0	2.32633
20	$\pi/6$	$4\pi/3$	3.00676	-3.00762	0.00027	2.41942	0.00016	2.27808
21	$\pi/6$	$11\pi/6$	3.01100	-3.01150	0.00014	2.46770	0.00011	2.23117

we can write the general solution (8) as a function of $(A_u, A_s, A_x, A_z, \phi_1, \phi_2)$:

$$\begin{aligned}
x(t) &= A_u e^{\lambda_1 t} + A_s e^{\lambda_2 t} + A_x e^{\eta_1 t} \cos(\omega_1 t + \phi_1) \\
&\quad + A_z e^{\eta_2 t} \bar{k}_5 \cos(\omega_2 t + \phi_2) + A_z e^{\eta_2 t} \bar{k}_6 \sin(\omega_2 t + \phi_2), \\
y(t) &= A_u k_1 e^{\lambda_1 t} + A_s k_2 e^{\lambda_2 t} + A_x e^{\eta_1 t} k_3 \cos(\omega_1 t + \phi_1) + A_x e^{\eta_1 t} k_4 \sin(\omega_1 t + \phi_1) \\
&\quad + A_z e^{\eta_2 t} k_5 \cos(\omega_2 t + \phi_2) + A_z e^{\eta_2 t} k_6 \sin(\omega_2 t + \phi_2), \\
z(t) &= A_u \bar{k}_1 e^{\lambda_1 t} + A_s \bar{k}_2 e^{\lambda_2 t} + A_x e^{\eta_1 t} \bar{k}_3 \cos(\omega_1 t + \phi_1) + A_x e^{\eta_1 t} \bar{k}_4 \sin(\omega_1 t + \phi_1) \\
&\quad + A_z e^{\eta_2 t} \cos(\omega_2 t + \phi_2),
\end{aligned} \tag{13}$$

or, in a more compact form,

$$\begin{aligned}
x(t) &= A_u e^{\lambda_1 t} + A_s e^{\lambda_2 t} + A_x e^{\eta_1 t} \cos(\omega_1 t + \phi_1) + A_z e^{\eta_2 t} \bar{k}_{56} \cos(\omega_2 t + \bar{\phi}_{56}), \\
y(t) &= A_u k_1 e^{\lambda_1 t} + A_s k_2 e^{\lambda_2 t} + A_x e^{\eta_1 t} k_{34} \cos(\omega_1 t + \phi_{34}) + A_z e^{\eta_2 t} k_{56} \cos(\omega_2 t + \phi_{56}), \\
z(t) &= A_u \bar{k}_1 e^{\lambda_1 t} + A_s \bar{k}_2 e^{\lambda_2 t} + A_x e^{\eta_1 t} \bar{k}_{34} \cos(\omega_1 t + \bar{\phi}_{34}) + A_z e^{\eta_2 t} \cos(\omega_2 t + \phi_2),
\end{aligned} \tag{14}$$

where the relations between the values of the parameters in (13) and in (14) are:

$$\begin{aligned}
k_{34} \cos \phi_{34} &= k_3 \cos \phi_1 + k_4 \sin \phi_1, & k_{34} \sin \phi_{34} &= k_3 \sin \phi_1 - k_4 \cos \phi_1, \\
\bar{k}_{34} \cos \bar{\phi}_{34} &= \bar{k}_3 \cos \phi_1 + \bar{k}_4 \sin \phi_1, & \bar{k}_{34} \sin \bar{\phi}_{34} &= \bar{k}_3 \sin \phi_1 - \bar{k}_4 \cos \phi_1, \\
k_{56} \cos \phi_{56} &= k_5 \cos \phi_2 + k_6 \sin \phi_2, & k_{56} \sin \phi_{56} &= k_5 \sin \phi_2 - k_6 \cos \phi_2, \\
\bar{k}_{56} \cos \bar{\phi}_{56} &= \bar{k}_5 \cos \phi_2 + \bar{k}_6 \sin \phi_2, & \bar{k}_{56} \sin \bar{\phi}_{56} &= \bar{k}_5 \sin \phi_2 - \bar{k}_6 \cos \phi_2.
\end{aligned}$$

Note that taking $A_u = A_s = 0$ in (14) produces a quasi-periodic solutions, Lissajous orbits, with frequencies ω_1 and ω_2 , and respective planar and vertical amplitudes equal to A_x and A_z . The values A_u and A_s are related to the unstable and stable manifold of the Lissajous orbit. For instance, the relation $A_u = 0$ and $A_s \neq 0$ defines the stable manifold of the Lissajous orbit defined by A_x and A_z ; any orbit verifying this condition will tend forward in time to the Lissajous orbit, since the term in A_s goes to zero. A similar fact happens when $A_u \neq 0$ and $A_s = 0$, in this case the term with A_u increases as time increases but goes to zero backwards in time, therefore, these solutions will go away exponentially fast forward in time, and define the unstable manifold of the Lissajous orbit.

3.2 The effective phases plane (EPP)

Following [26], to describe Lissajous orbits is very convenient to use the so called effective phases (Φ, Ψ) . They are an adaptation of the action-angle variables to describe states on invariant tori in dynamical systems that can characterize very well heteroclinic connections [29, 30]. A Lissajous trajectory is determined by two amplitudes A_x, A_z and two phases, ϕ_1 and ϕ_2 , at $t = 0$. The effective phases are defined by:

$$\begin{aligned}\Phi(t) &= \omega_1 t + \phi_1 \pmod{2\pi}, \\ \Psi(t) &= \omega_2 t + \phi_2 \pmod{2\pi}.\end{aligned}$$

Clearly, at each epoch, t , there is a one-to-one correspondence between a pair of effective phases $(\Phi(t), \Psi(t)) \in [0, 2\pi] \times [0, 2\pi]$ and the state $(x(t), y(t), z(t), \dot{x}(t), \dot{y}(t), \dot{z}(t))$ on the Lissajous. Using this representation, the 2D tori defined by Lissajous orbits become straight lines with slope ω_1/ω_2 (a value slightly less than one in our case) in the effective phases plane $[0, 2\pi] \times [0, 2\pi]$. The orbit at $t = 0$ departs from the point (ϕ_1, ϕ_2) and travels with constant velocity components ω_1 and ω_2 in the EPP. Note that each point (Φ, Ψ) on the EPP identifies a position on the Lissajous orbit, although the size of current the orbit, given by the constant values A_x and A_z , is not represented. When the orbit is on a stable or unstable manifold either A_u or A_s has a non-zero constant value, but the purpose of the EPP remains the same.

For one of the transfers between two Lissajous orbits that are computed in the next sections, Fig 4 shows how the departing (in blue) and arrival (in black) orbits are seen in both, the configuration space and in the EPP. The left plot shows, in the configuration space, the departing (in blue) and arrival (in black) orbits. The other two plots correspond to the EPP representation of the departing (middle) and arrival (right) orbits. The red cross in the departure EPP indicates the starting position, while the one in the arrival EPP indicates the maneuver insertion in the stable manifold of the arrival orbit. More applications will be shown in the following sections.

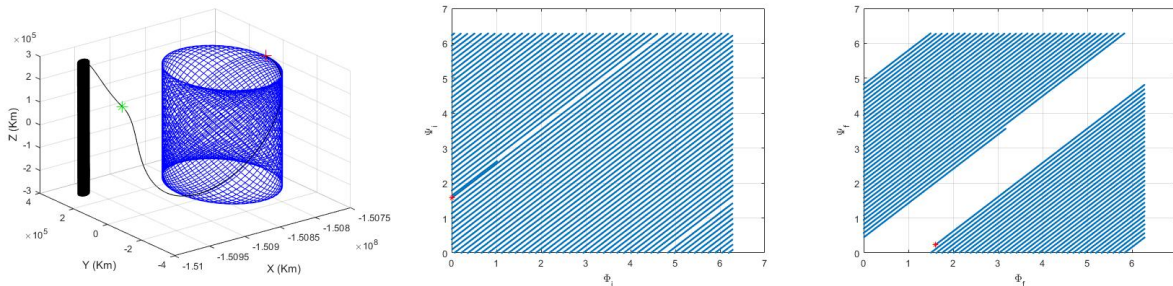


Figure 4: Transfer between two Lissajous orbits in the configuration space and in the EPP.

4 Heteroclinic enhanced connections between Lissajous orbits

This section is devoted to introduce the SRP maneuver strategy that defines the heteroclinic enhanced connections between libration point orbits around the collinear equilibrium points. These transfers are propellant-free and are performed by means of a variation of the sail parameters: α (cone angle), δ (clock angle) or β (lightness number). The influence of the phases ϕ_1 and ϕ_2 at the departing point, as well as the amplitudes A_x and A_z of the initial orbit, will be also analyzed.

As we have seen, the stability and location of the SRP-libration points change with the sail parameters, for this reason we use three different reference systems to design a transfer. The first is usual CR3BP synodic frame (X, Y, Z) centered on the Sun-Earth center of mass. The second and third ones are respectively associated with the departure and target libration points and we denote by (x, y, z) and (x', y', z') their coordinates. The three reference systems are related by the change of variables:

$$\begin{cases} X = \gamma x + \gamma_1 = \gamma x' + \gamma'_1, \\ Y = \gamma y + \gamma_2 = \gamma y' + \gamma'_2, \\ Z = \gamma z + \gamma_3 = \gamma z' + \gamma'_3, \\ \dot{X} = \gamma \dot{x} = \gamma \dot{x}', \\ \dot{Y} = \gamma \dot{y} = \gamma \dot{y}', \\ \dot{Z} = \gamma \dot{z} = \gamma \dot{z}', \end{cases} \quad (15)$$

where $(\gamma_1, \gamma_2, \gamma_3)$ and $(\gamma'_1, \gamma'_2, \gamma'_3)$ are the coordinates of the departure and target SRP libration points in the CR3BP reference system, and $\gamma = 0.01$, is a convenient scaling factor introduced to normalize the Earth-equilibrium point distance (using this scaling factor the distance from the Earth to the SL_2 point in the local reference frames is approximately one, corresponding to about 1.5×10^6 km in physical units). In Fig. 5 we schematically show the three reference systems involved when, by means of a solar-sail maneuver, we intend to connect a LPO around SL_2 with another one around SL'_2 .

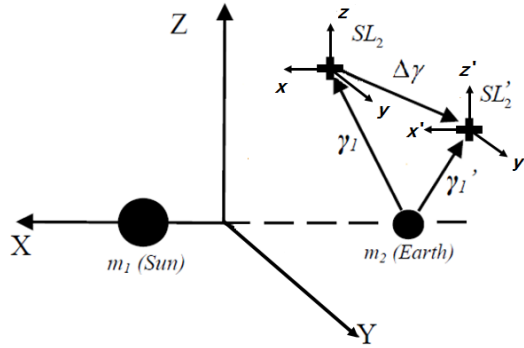


Figure 5: Schematic representation of the three reference systems involved in the study of solar-sail maneuvers. Due to the maneuver, the equilibrium point moves from SL_2 (position before the maneuver) to SL'_2 (position after the maneuver).

An interesting dynamical remark on solar-sail maneuvers using always these SL_i centered local reference frames is that, contrary to usual impulsive maneuvers that involve a change in velocities (known as a Δv), the solar-sail maneuver changes the position coordinates of the artificial equilibrium point but keeps the velocity. So it can be assumed as a jump in position in the (lowercase) local frame, although in the usual CR3BP the orbit is continuous in both position and velocity.

Assuming that we are departing from a Lissajous orbit by means of a trajectory on its unstable manifold, we accomplish an heteroclinic enhanced connection by means of a solar-sail maneuver that injects us on the stable manifold of the target one. In what follows, we study the characteristics of these transfers considering:

- Maneuvers that change of the cone angle α of the sail.
- Maneuvers that change of the clock angle δ of the sail.
- Maneuvers that change the lightness number β of the sail.
- Dependency on the phases, ϕ_1 and ϕ_2 , of the departing point.
- Dependency on the amplitudes of the departing Lissajous orbit.

4.1 Heteroclinic enhanced connections changing the cone angle for a fixed ϕ_1 and ϕ_2

We note that to obtain such connection between two Lissajous orbits, the unstable component, A_u , of the arrival one should be equal to zero after the solar-sail maneuver. In this section, we explore the changes of the cone angle α that fulfill this arrival condition. For all the computations that follow we keep fixed the value of the clock angle $\delta = \pi/2$,

the lightness number $\beta = 0.02$, the phases of the departing point $\phi_1 = \phi_2 = 0$, and the size of the departing orbit, given by the normalized amplitudes $A_x = 1/24$ and $A_z = 1/6$.

Since the departure of the initial Lissajous orbit is done along its unstable manifold, we must set the amplitudes $A_s = 0$ and $A_u \neq 0$; we have used $A_u = -10^{-4}$. Fixing the values of the phases ϕ_1 and ϕ_2 at $t_0 = 0$ we are selecting an orbit of the unstable manifold of the Lissajous orbit, the whole manifold can be obtained varying the values of these phases. Along the selected orbit on the unstable manifold we consider a fixed time step of $\Delta t = 10^{-4}$ adimensional time units, for a maximum time interval of $t_{max} - t_0 = 15$ adimensional time units. At each time step we consider a potential change in the cone angle from its initial value α_i to a final one α_f . This means that the cone angle variation we consider is always equal to $\Delta\alpha = \alpha_f - \alpha_i$. Then, we compute the unstable component of the resulting trajectory associated to the new sail parameters in order to check for the condition $A'_u = 0$, that guarantees that we are on the stable manifold of a Lissajous orbit. The computations are done according to the following scheme:

1. Initialize the parameters: $\mu, \alpha_i, \alpha_f, \delta, \beta, \phi_1 = \phi_2 = 0, t_0 = 0, \Delta t, t_{max}$, and the amplitudes A_x and A_z (from which ones we can compute A_3, A_4, A_5 and A_6 using the relations (12)).
2. Set $A_1 = A_u = -10^{-4}, A_2 = A_s = 0$, and $t = t_0 = 0$.
3. Set $\alpha = \alpha_i$, and compute the coordinates $(\gamma_1, \gamma_2, \gamma_3)$ of the equilibrium point.
4. Using the expressions given in Appendix A, compute the coefficients of the polynomial (4), and its roots: $\lambda_1, \lambda_2, \lambda_{3,4} = \eta_1 \pm \omega_1 i, \lambda_{5,6} = \eta_2 \pm \omega_2 i$.
5. Using the expressions given in Appendix C, compute the matrix $H(t)$ and determine the state $(x, y, z, \dot{x}, \dot{y}, \dot{z})$ at time t .
6. Change α_i to α_f and compute the position of the new artificial equilibrium point $(\gamma'_1, \gamma'_2, \gamma'_3)$, as well as $(x', y', z', \dot{x}', \dot{y}', \dot{z}')$ by means of (15).
7. Since the vectorfield is autonomous, we can use (11) to get the values of the resulting amplitudes $A'_1 = A'_u, A'_2 = A'_s, A'_3, A'_4, A'_5, A'_6$ after the maneuver.
8. Store the values of t and the obtained unstable amplitude A'_u .
9. Set $t = t + \Delta t$ and, if $t < t_{max}$, go to step 5.

We have always taken an initial cone angle $\alpha_i = 0$, so the cone angle maneuver is $\Delta\alpha = \alpha_f - \alpha_i = \alpha_f$.

4.1.1 Evolution of the final unstable amplitude for positive and negative cone angle maneuvers

The analysis of the results is divided into two cases: $\Delta\alpha = \alpha_f > 0$ and $\Delta\alpha = \alpha_f < 0$. For both cases, Fig. 6 shows a typical evolution of A'_u as a function of the maneuver time (this is the time where the value of α changes from $\alpha_i = 0$ to α_f). In the plots of the figure, each line represents a different value of $\Delta\alpha = \alpha_f$. The values that have been explored are $\Delta\alpha \in (0.01, \pi/2)$ (left plot) and $\Delta\alpha \in (-0.01, -\pi/2)$ (right plot).

From the left plot of the figure it follows that, for any fixed value of $\alpha_f > 0$, there is only one value of the maneuver time for which A'_u is zero. These values will be the suitable epochs (after departure) to perform the transfer maneuver by means of a change of the cone angle.

As an example, Fig. 7 shows the transfer connection associated to $\Delta\alpha = \pi/4$. The solar-sail maneuver is performed after 1.9 adimensional time units after the departure from the initial Lissajous orbit (in blue). The red cross indicates the departing point along the unstable manifold of the initial orbit, and the green cross the place of the maneuver, from this point on the orbit follows an orbit on the stable manifold of the arrival Lissajous orbit (in black).

From the right panel of Fig. 6 we find that, when $\Delta\alpha = \alpha_f < 0$, there are four different behaviors, according to the number of crossings with the $A'_u = 0$ axis of the lines associated to different α_f values. The curves $A'_u(\alpha_f)$ displayed in the figure have zero crossings with $A'_u = 0$ when $\alpha_f \in (-0.22, -0.01)$, one crossing when $\alpha_f \in (-\pi/2, -0.51)$, two crossings when $\alpha_f \in (-0.40, -0.23)$ and three crossings when $\alpha_f \in (-0.50, -0.41)$. In Fig. 8 we show one example of each case and in Fig. 9 we show the resulting connections obtained for each case (3D (X, Y, Z) CR3BP representation

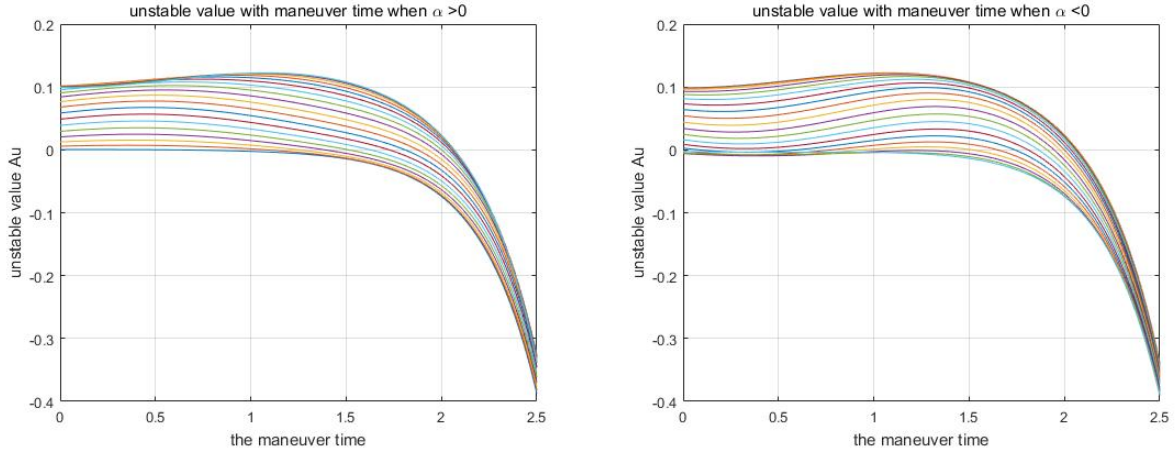


Figure 6: Behavior of A'_u vs maneuver time for $\Delta\alpha = \alpha_f \in (0.01, \pi/2)$ (left) and for $\Delta\alpha = \alpha_f \in (-0.01, -\pi/2)$ (right).

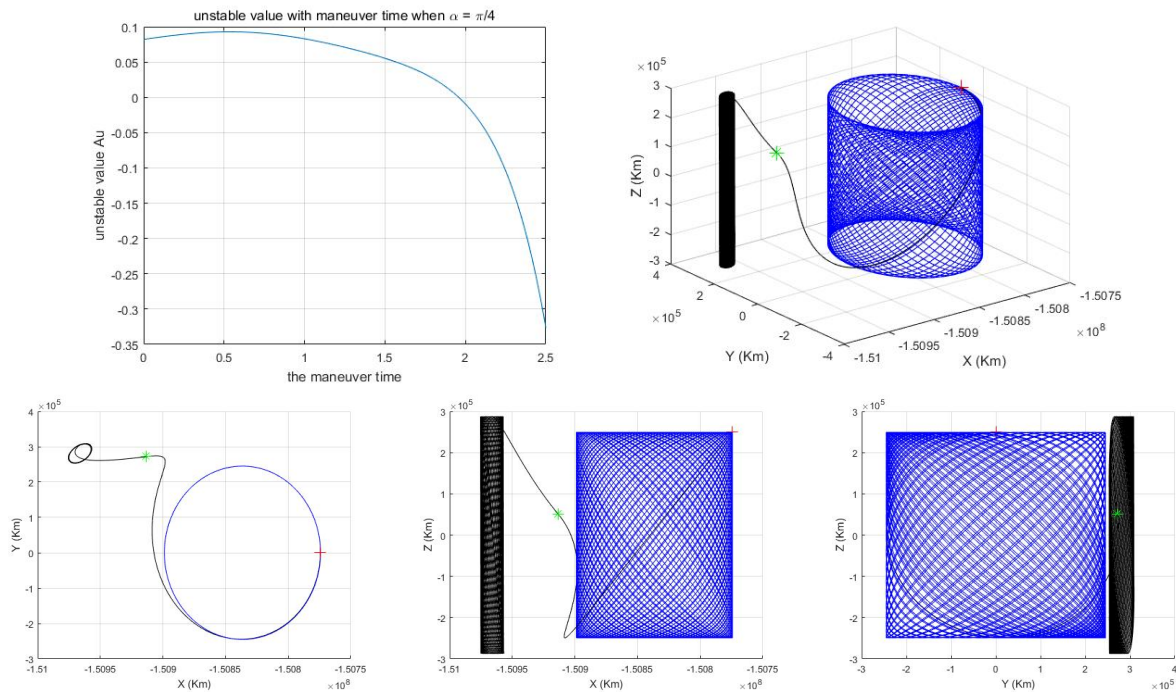


Figure 7: Evolution of the final unstable amplitude A_u for $\alpha_f = \pi/4$ (top left), 3D representation and coordinate projections of the initial (in blue) and final (in black) Lissajous orbits. The orbit plots are in the (X, Y, Z) CR3BP reference frame, but using physical units (km).

and XY -projections using physical units in km) of the initial (in blue) and final (in black) Lissajous orbits associated to the transfers determined for $\alpha_f = -\pi/4$ (one $A'_u = 0$ crossings), $\alpha_f = -0.35$ (two $A'_u = 0$ crossings), and $\alpha_f = -0.45$ (three $A'_u = 0$ crossings).

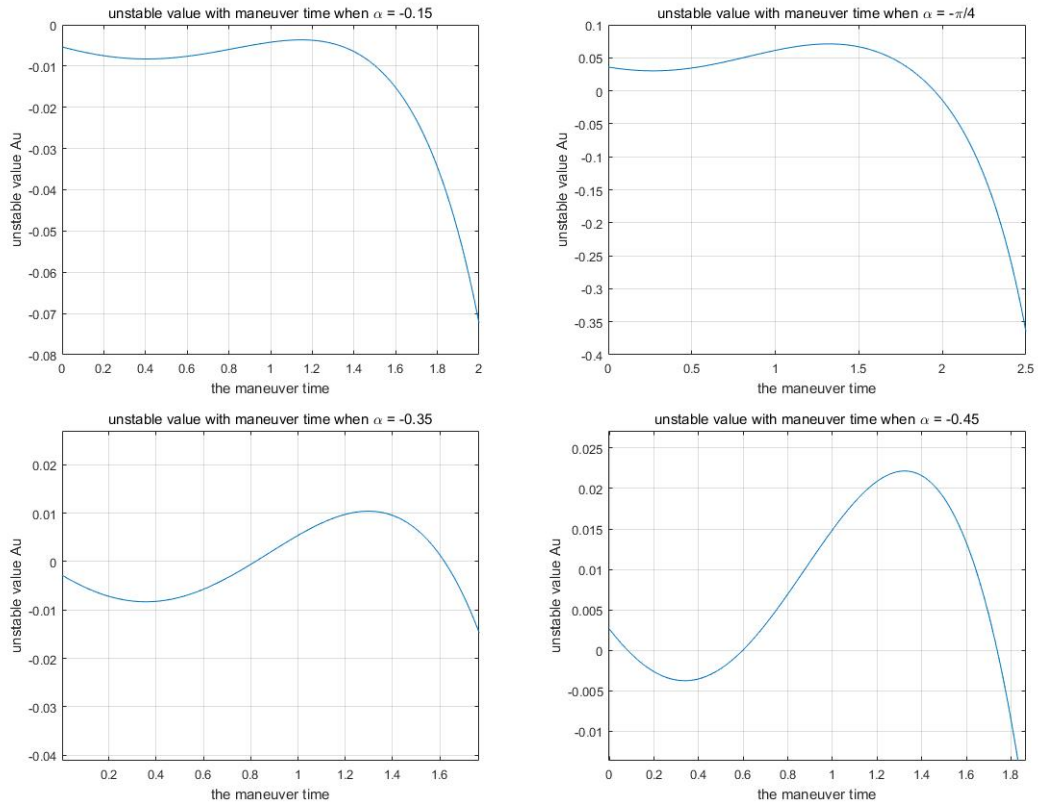


Figure 8: Behavior of A'_u vs maneuver time for $\alpha = -0.15$ (zero crossings with $A'_u = 0$), $\alpha_f = -\pi/4$ (one crossing), $\alpha_f = -0.35$ (two crossings), $\alpha_f = -0.45$ (three crossings).

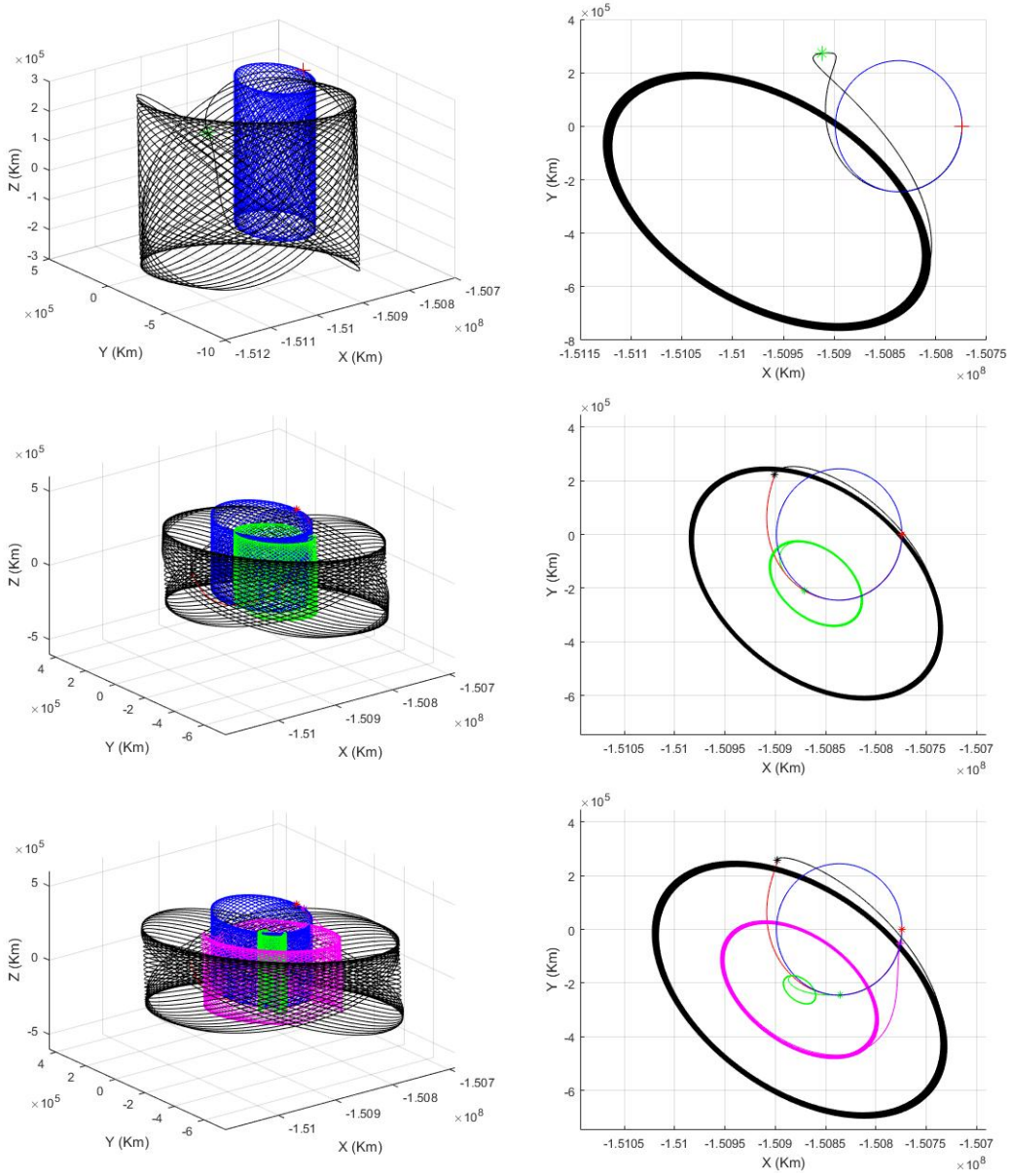


Figure 9: 3D representation and XY -coordinate projection for the three different cases with existing connections of Fig 8. The departure Lissajous is represented in blue.

In the following we give some details about the behavior of the transitions between these three different situations.

1. When α_f varies between -0.52 and -0.50 , the number of connections goes from 1 to 3, since in this interval the curve $A'_u(\alpha_f)$ goes through a tangency with the $A'_u = 0$ line for $\alpha_f \approx -0.51$. Fig. 10 shows the behavior of A'_u as a function of the maneuver time for this value of α_f .
2. When α_f varies between -0.42 and -0.40 , the number of connections goes from 3 to 2, since in this interval the curve $A_u(\alpha_f)$ goes through a tangency with the $A_u = 0$ line for $\alpha_f \approx -0.41$.
3. When α_f varies between -0.23 and -0.20 , the number of connections goes from 2 to 0, since in this interval the curve $A'_u(\alpha_f)$ goes through a tangency with the $A'_u = 0$ line for $\alpha_f \approx -0.20$.

Table 2 gives the values of the maneuver time and amplitudes of the Lissajous final orbits in physical units, and Fig. 10 shows the departing and final Lissajous orbits together with the transfer path that follows the unstable manifold of the departing orbit, until the maneuver time, and the stable manifold of the final one.

Table 2: Maneuver time and Lissajous final amplitudes of the connections close to the tangencies with $A'_u = 0$ for negative cone angle maneuvers.

α_f	Maneuver time (days)	Final X-amplitude A'_x (10^6 km)	Final Z-amplitude A'_z (10^6 km)
-0.51	104.2	14.8	26.78
-0.50	15.06	5.1	25.58
-0.50	23.08	2.8	26.18
-0.50	103.7	14.7	26.63
-0.41	0.39	8.15	24.94
-0.41	40.20	2.82	26.15
-0.41	98.66	13.35	25.96
-0.40	41.46	3.13	26.07
-0.40	98.00	13.17	25.88
-0.23	68.06	7.48	24.95
-0.23	75.12	8.42	24.94

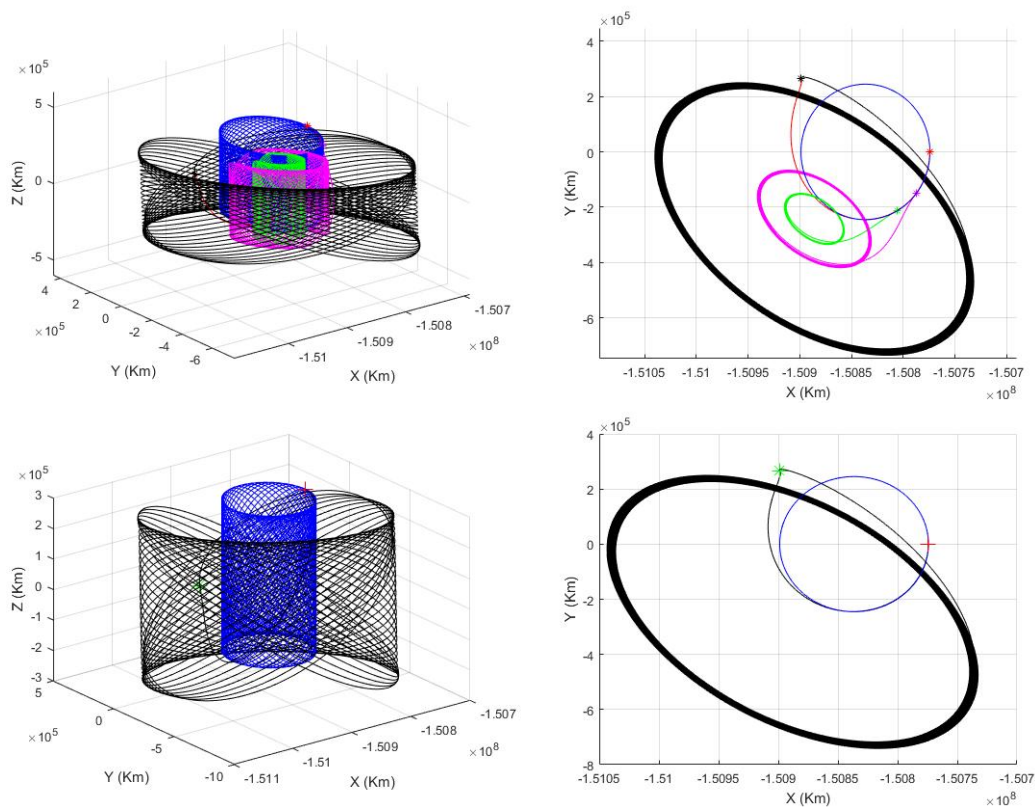


Figure 10: Departing (blue) and final Lissajous (green, magenta, and black) orbits, together with the connecting path in the unstable manifold of the departing orbit (before the maneuver) and in the stable manifold of the final one (after the maneuver). The results correspond to $\alpha_f \in (-0.51, -0.50)$.

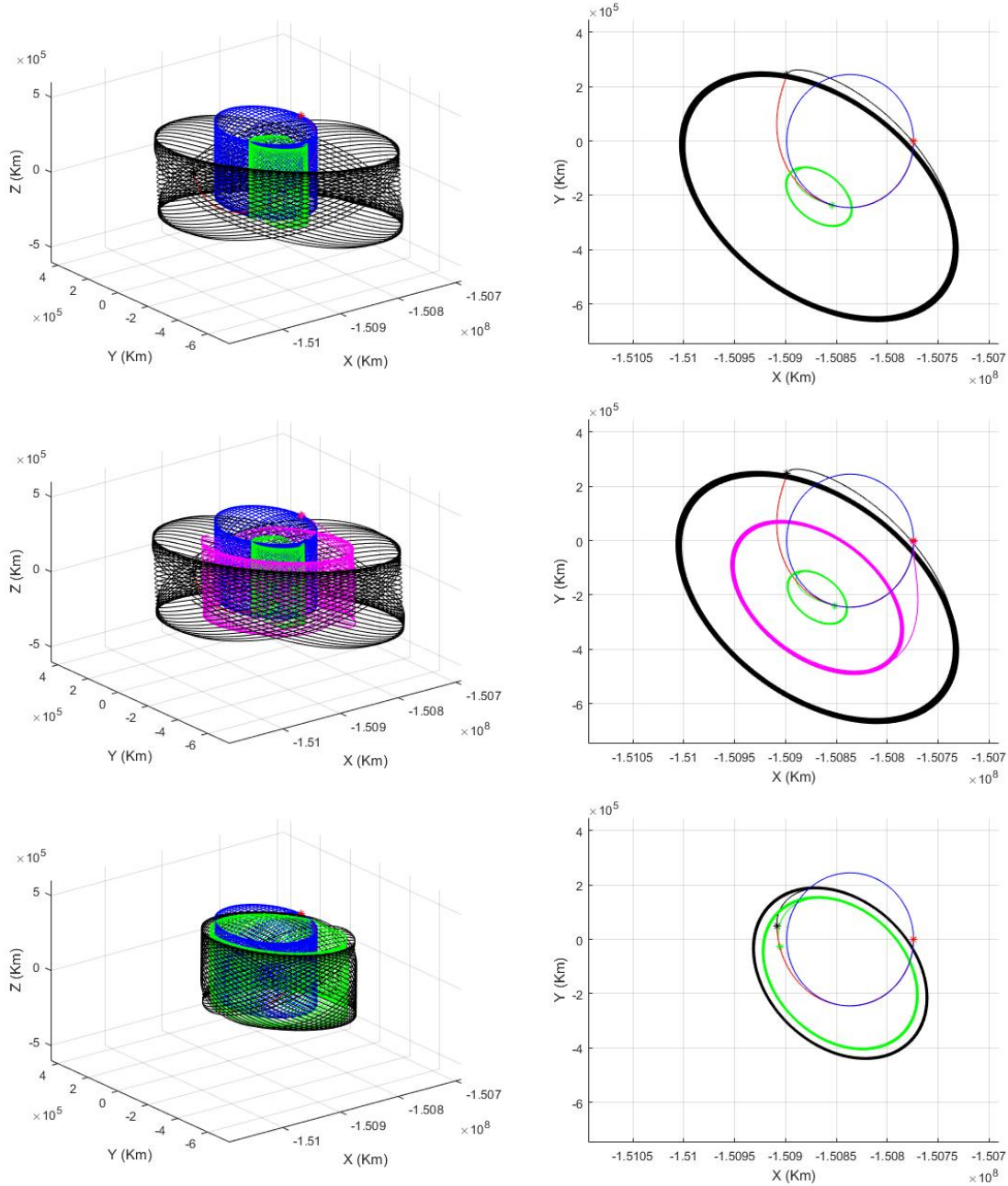


Figure 11: Same as Fig. 10 but for $\alpha_f \in (-0.41, -0.40)$ (first two rows) and $\alpha_f = -0.23$ (bottom row).

4.1.2 Evolution of the planar and vertical amplitudes of the final Lissajous orbits for cone angle maneuvers

We have seen how to perform a transfer from a given Lissajous orbit changing the cone angle parameter of the sail and keeping fixed the remaining sail parameters. Next we show how the X and Z amplitudes, A'_x and A'_z respectively, of the reached Lissajous orbit, as well as the epoch of the maneuver, depend on $\Delta\alpha$. The results obtained are given in Fig. 12. As it has already been said, for $\alpha \in (-0.22, -0.01)$ there is a gap associated to the fact that for these values of α the unstable amplitude A'_u does not intersect the $A'_u = 0$ line. In the top plots we show the amplitudes, A'_x, A'_z of the final Lissajous orbit as a function of the cone angle maneuver $\Delta\alpha$. The bottom plot shows the value of the epoch of the maneuver after the departure also as a function of the cone angle maneuver $\Delta\alpha$. When $\Delta\alpha = \alpha_f \in (-0.22, -0.01)$ there are no connections since for these values $A'_u \neq 0$.

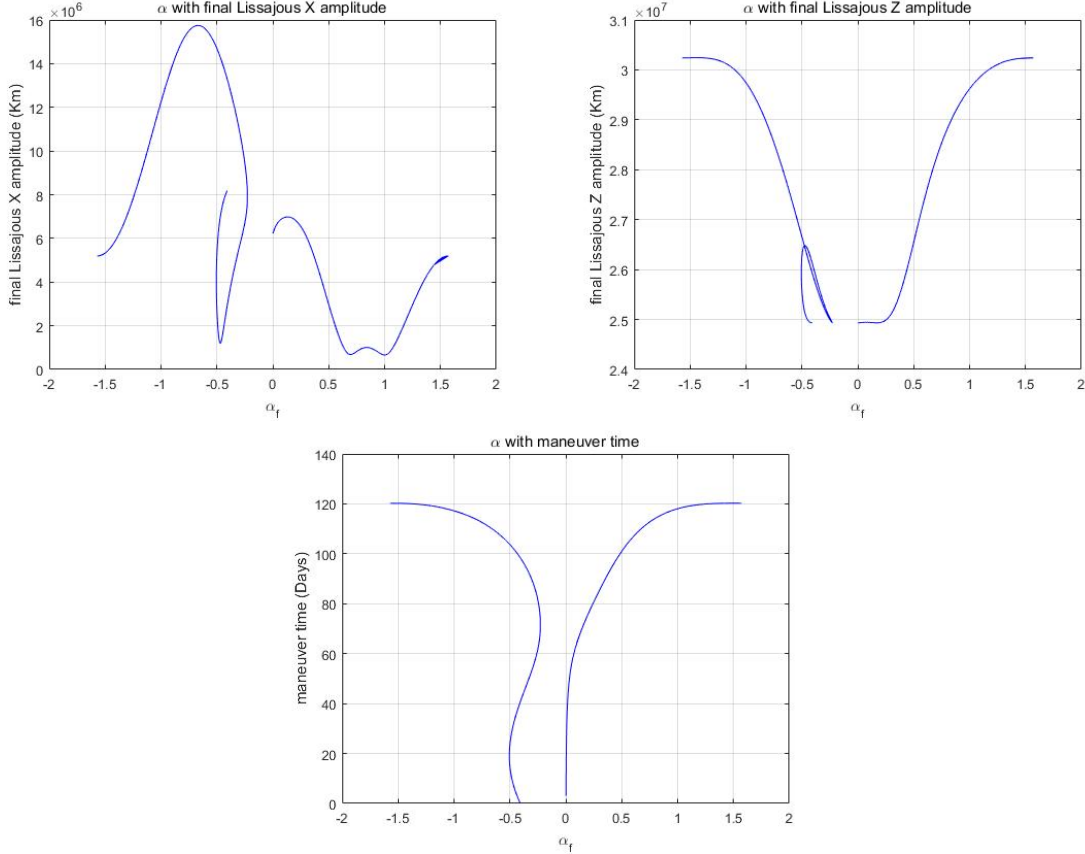


Figure 12: Final cone angle with X,Z Amplitudes and maneuver time.

4.1.3 Evolution of the maneuver time when $\alpha_i \neq 0$

In the previous computations we have set equal to zero the value of the cone angle before the maneuver ($\alpha_i = 0$); when this angle changes the maneuver time also does. Next we show how this time changes when α_i varies within its range, $(-\pi/2, \pi/2)$, keeping fixed the values of the remaining parameters: $\delta = \pi/2$, $A_s = 0$, $A_u = -10^{-4}$, $A_x = 1/24$, $A_z = 1/6$, and $\phi_1 = \phi_2 = 0$.

Figs. 13 and 14 show the results obtained when $\alpha_i \in (0, \pi/2)$. Note that in the plots of both figures $\alpha_f \in (0, \pi)$ instead of $\alpha_f \in (-\pi/2, \pi/2)$, so the results for $\alpha_f \in (\pi/2, \pi)$ are, in fact, the ones for $\alpha_f \in (-\pi/2, 0)$. This is because the maneuver time for $\alpha_f = -\pi/2$ coincides with the one for $\alpha_f = \pi/2$.

As in the case $\alpha_i = 0$, we have also that, depending on the value of $\Delta\alpha = \alpha_f - \alpha_i$, there are 0, 1 2 or 3 possible transfer times, giving $A'_u = 0$ after the the maneuver. For all possible values of α_i we get values of the solar-sail time maneuver very close to zero, which means that we can perform a transfer without using the unstable orbit of the departing Lissajous orbit. When $\alpha_i > 1.087$ it appears a gap in the possible values of the transfer time around $t_{trans} = 0.7$.

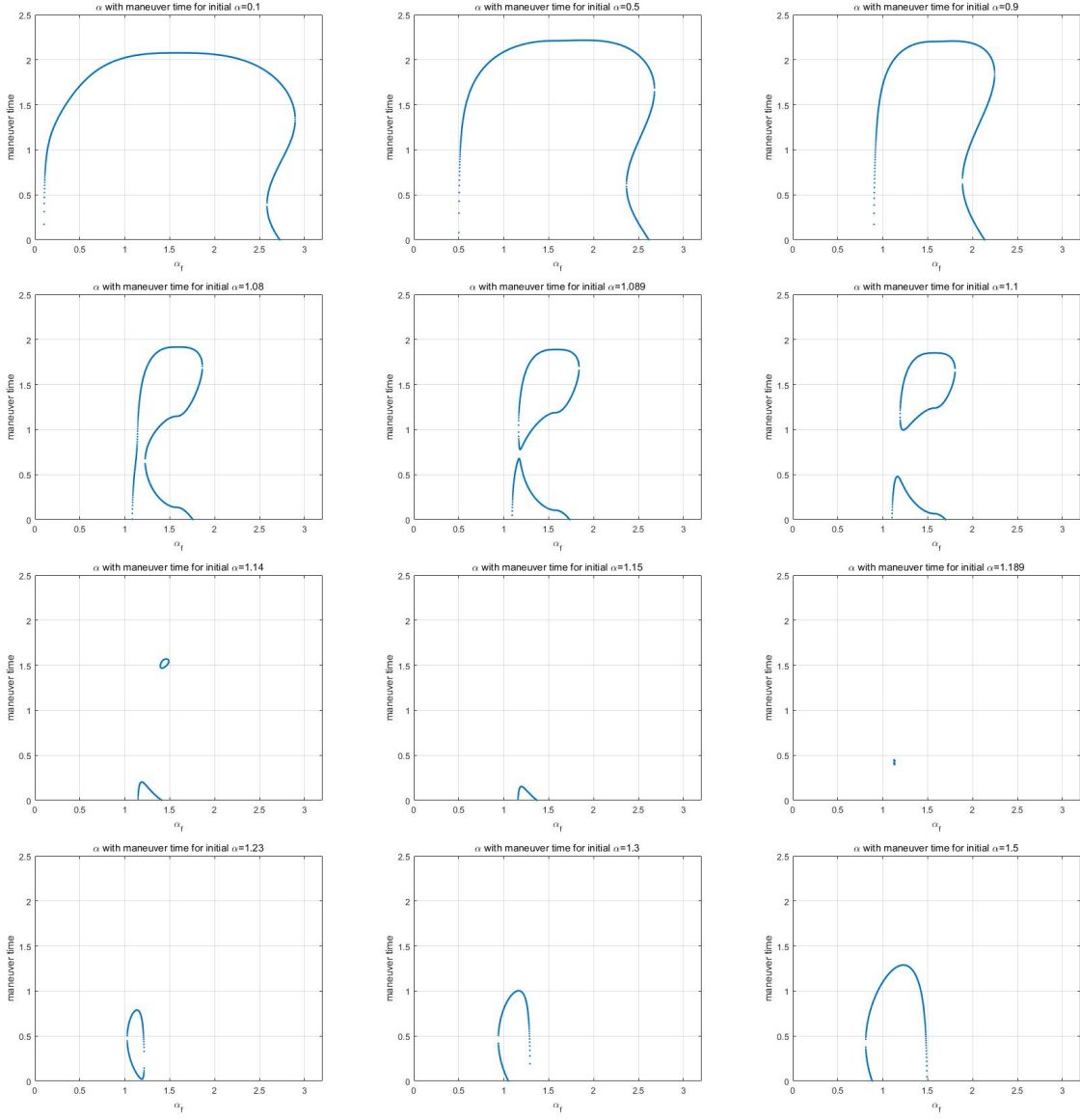


Figure 13: Maneuver time as a function of α_f , for different initial cone angles $\alpha_i \in (0, \pi/2)$. The applied maneuver is $\Delta\alpha = \alpha_f - \alpha_i$.

The size of the gap increases, and for $\alpha_i \in (1.186, 1.189)$ there are no possible transfers. Transfer possibilities appear again for $\alpha_i = 1.189$. From this value on, the corresponding maximum maneuver time increases until the α_i equals to $\pi/2$. Note that the range of the possible maneuver values $\Delta\alpha = \alpha_f - \alpha_i$ also varies with α_i .

Finally, Fig. 15 shows the maneuver times and the final X and Z amplitudes, when both the initial and final cone angles α_i and α_f vary in $(-\pi/2, \pi/2)$. The right bottom plot of this figure is the projection on the $\alpha_i - \alpha_f$ plane of the three above plots. Note that this projection has three unconnected regions: the smaller region on the right is related to the gap already mentioned for $\alpha_i > 1.087$, the other two regions correspond to $\alpha_f < \alpha_i$ (lower region), and $\alpha_f > \alpha_i$ (upper region).

4.2 Heteroclinic enhanced connections when varying the cone angle and the phases ϕ_1 and ϕ_2

In the previous section we studied connections associated to changes of the cone angle for initial phases $\phi_1 = \phi_2 = 0$, which means that only one orbit of the unstable manifold of the departing Lissajous orbit is considered. Next we allow variations in both phases in order to explore the full unstable manifold of the Lissajous orbit, enlarging this way the

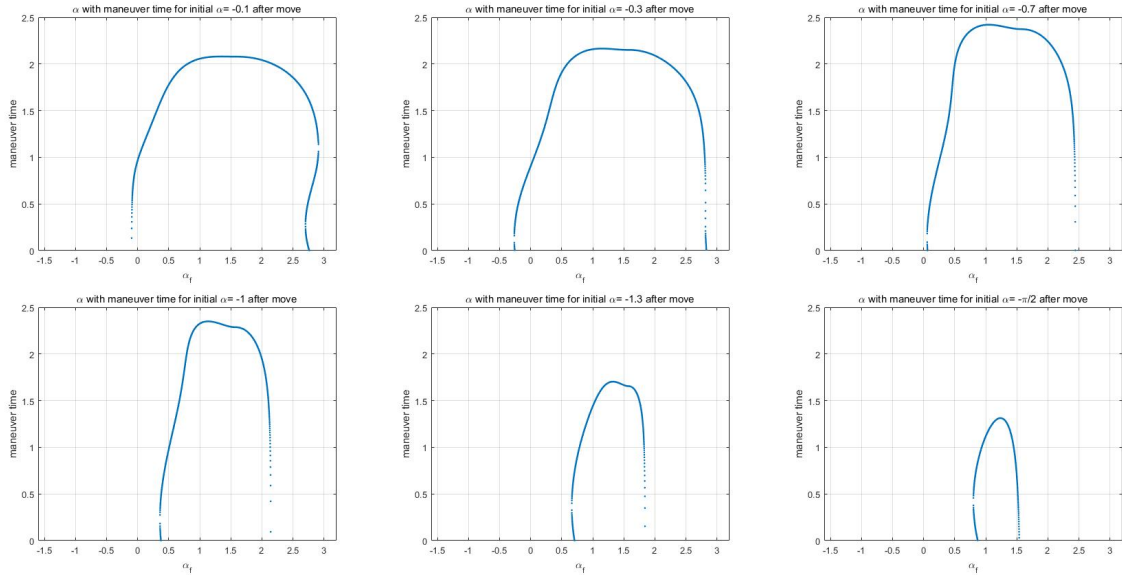


Figure 14: Maneuver time as a function of α_f , for different initial cone angles $\alpha_i \in (-\pi/2, 0)$.

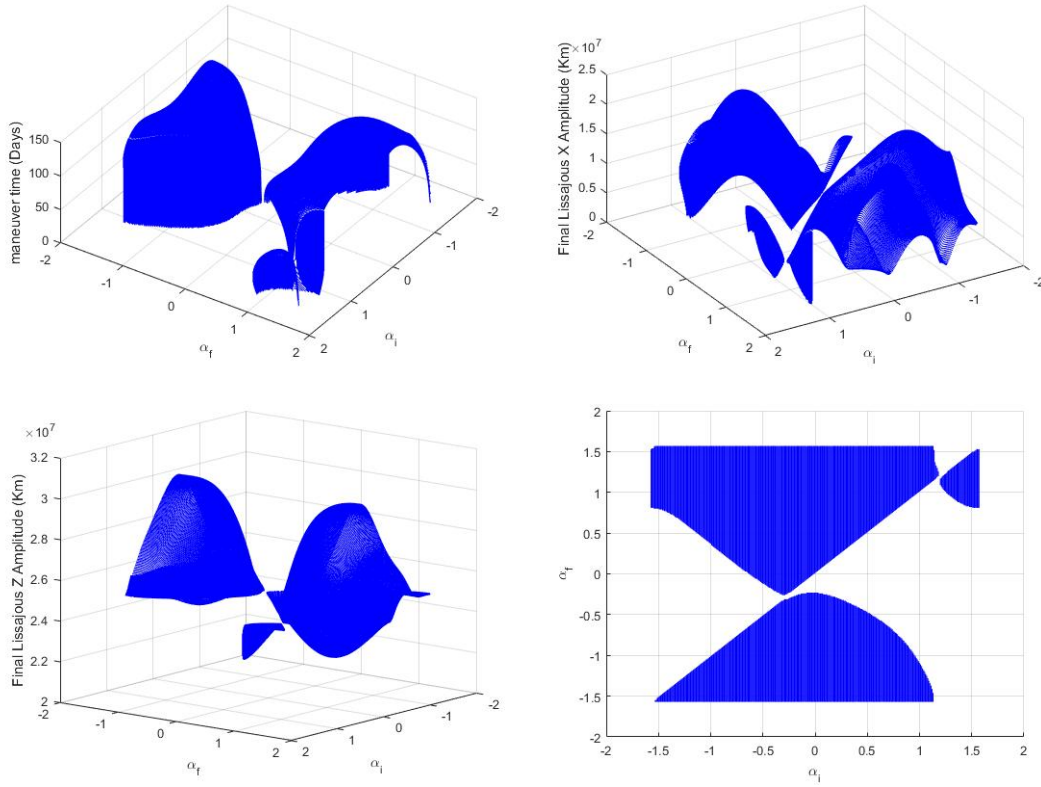


Figure 15: Maneuver times, and final X and Z amplitudes as a function of the initial and final cone angles α_i and α_f .

transfer possibilities.

As in the preceding section, for all the explorations that follow we fix the initial and final values of the clock angle $\delta = \pi/2$, as well as the size of the departing orbit, given by the amplitudes $A_x = 1/24$ and $A_z = 1/6$ in normalized units.

4.2.1 Evolution of the final Lissajous parameters with respect to ϕ_1 and ϕ_2

With the above mentioned parameters, together with $\alpha_i = 0$, $\alpha_f = \pi/4$, keeping fixed $\phi_2 = 0$, and varying $\phi_1 \in (-\pi/2, 3\pi/2)$, for each value of ϕ_1 there is only one possible connection. Fig. 16 shows the values of the maneuver time as well as the X and Z amplitudes of the final Lissajous orbit reached with the solar-sail maneuver.

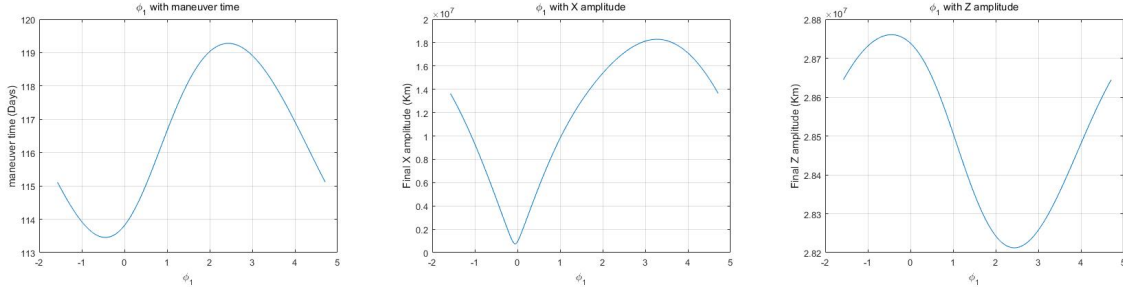


Figure 16: Maneuver times and final X and Z amplitudes, when $\phi_1 \in (-\pi/2, 3\pi/2)$ and $\phi_2 = 0$.

If instead of keeping fixed $\phi_2 = 0$ we fix $\phi_1 = 0$ and vary $\phi_2 \in (-\pi/2, 3\pi/2)$, for each value of ϕ_2 there is only one possible connection when, as before, $\alpha_i = 0$ and $\alpha_f = \pi/4$. Fig 17 shows the maneuver times as well as the X and Z amplitudes of the final Lissajous orbit reached with the solar-sail maneuver. Clearly in this case, the variation of ϕ_2 does not affect the maneuver time and the final X -amplitude; only the Z -amplitude of the final Lissajous orbits varies.

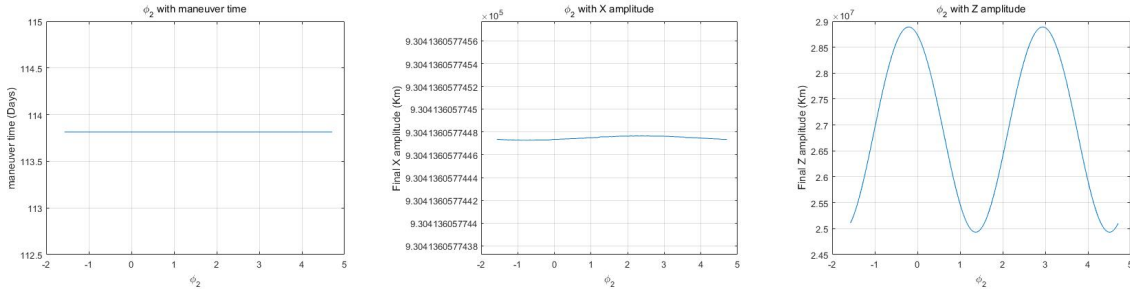


Figure 17: Maneuver times and final X and Z amplitudes, when $\phi_1 = 0$ and $\phi_2 \in (-\pi/2, 3\pi/2)$.

When the condition $\alpha_f = \pi/4$ is removed, allowing α_f to vary in $(-\pi/2, \pi/2)$, Figs. 18 and 19 show the values of the maneuver time, as well as the X and Z amplitudes of the final Lissajous orbit, for $\phi_1 \in (-\pi/2, 3\pi/2)$, $\phi_2 = 0$ and $\phi_1 = 0$, $\phi_2 \in (-\pi/2, 3\pi/2)$, respectively. Each transfer corresponds to different values of (α_f, ϕ_1) in the first figure, and of (α_f, ϕ_2) in the second one. Fig. 19 shows that the variations of ϕ_2 only modify the final Z amplitude, not affecting the maneuver time and the final X amplitude.

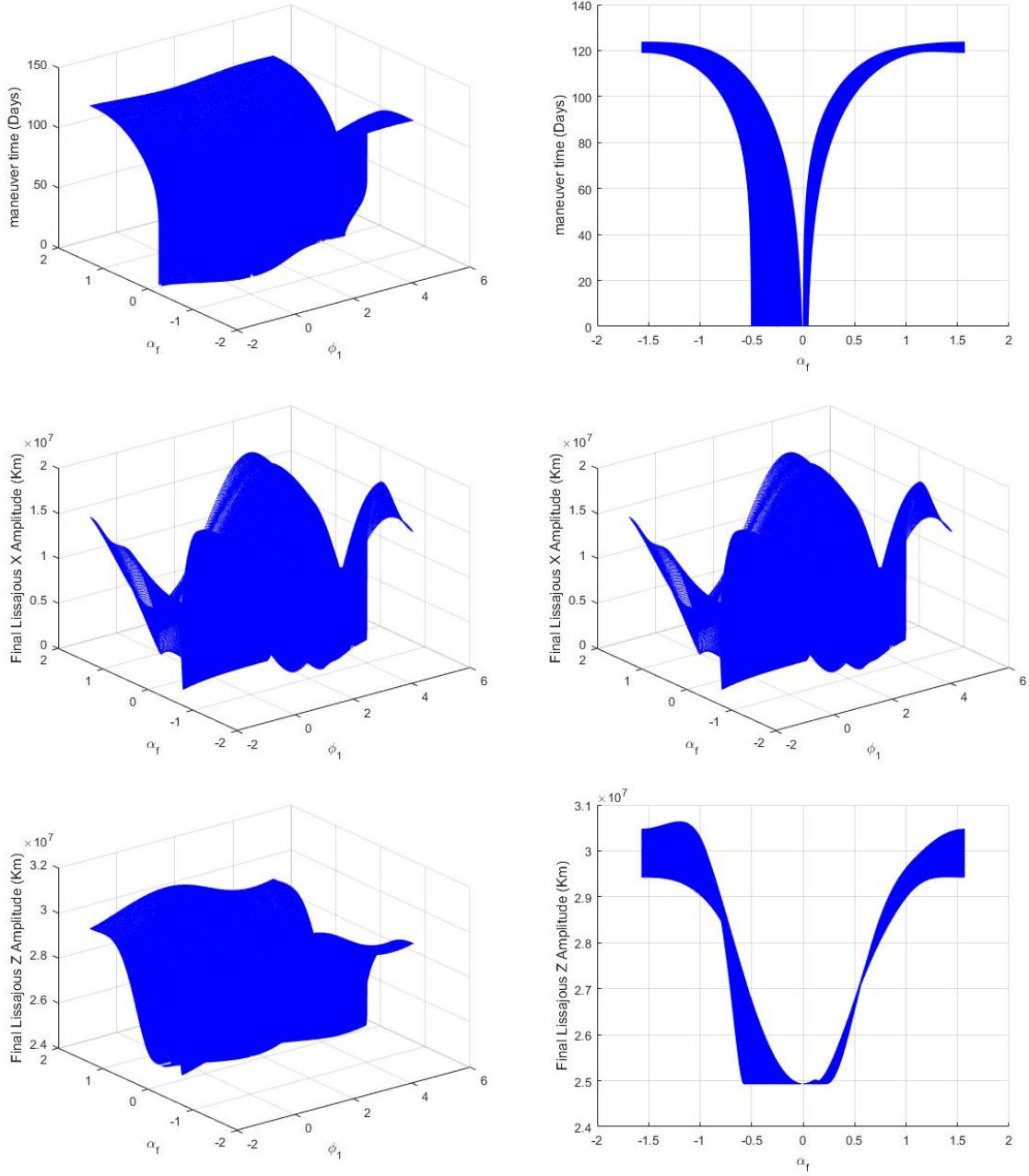


Figure 18: Maneuver time s (top) and final X (middle) and Z (bottom) amplitudes, when $\phi_1 \in (-\pi/2, 3\pi/2)$, $\phi_2 = 0$ and $\alpha_f \in (-\pi/2, \pi/2)$.

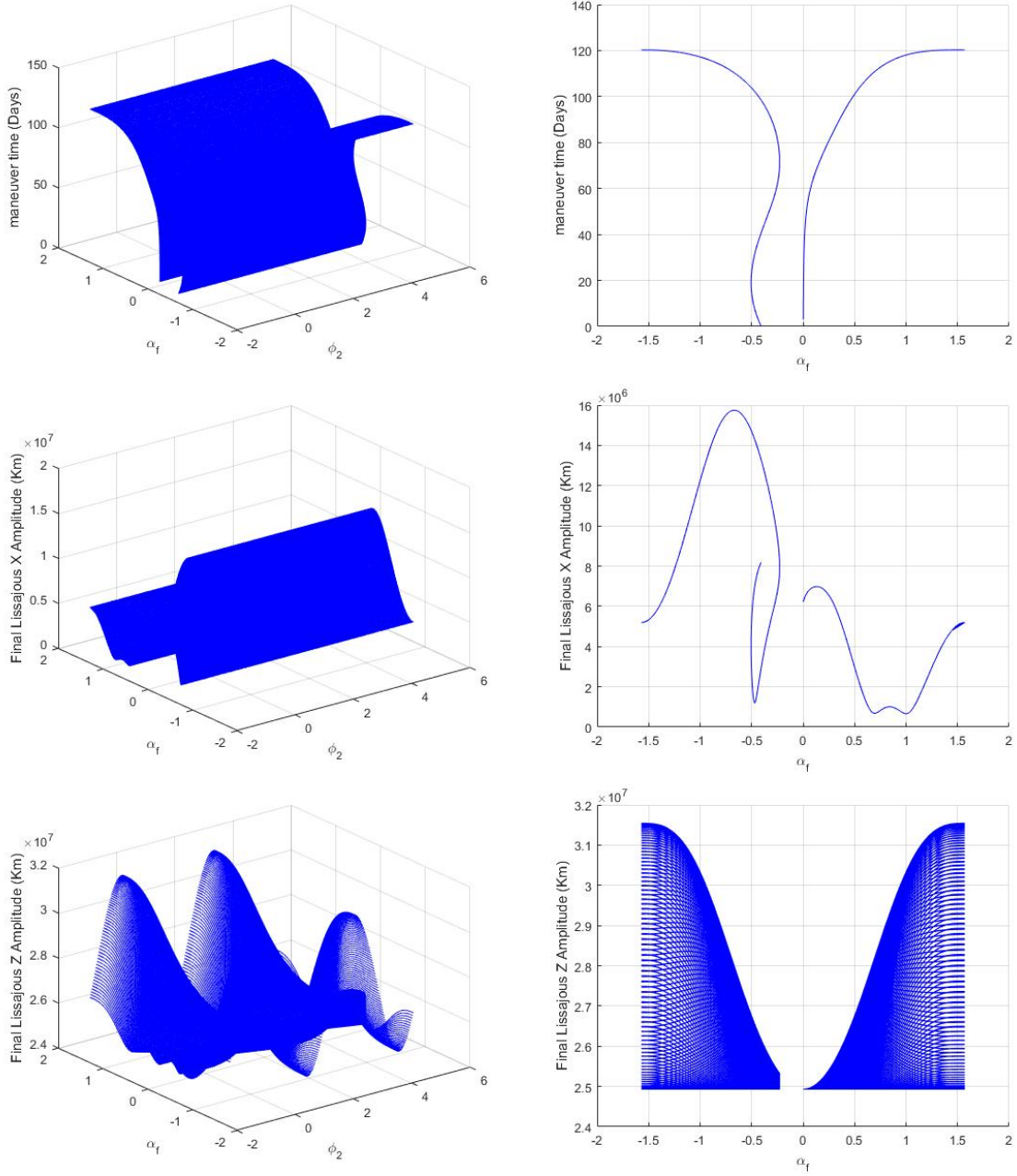


Figure 19: Maneuver times (top) and final X (middle) and Z (bottom) amplitudes , when $\phi_1 = 0$, $\phi_2 \in (-\pi/2, 3\pi/2)$, and $\alpha_f \in (-\pi/2, \pi/2)$.

It is worth to remark that, due to the symmetry of the solutions with respect to the $z = 0$ plane, the same final Lissajous orbit can be reached departing from two different points of the initial one, by changing only the value of the phase ϕ_2 into $\phi_2 + \pi$, and in fact, the two transfer times are also the same. Fig. 20 shows the two connections obtained when departing from a Lissajous orbit with $A_x = 1/24$, $A_z = 1/6$, $\phi_1 = 0$ and ϕ_2 values $\phi_2 = 0$, $\phi_2 = \pi$. For both connections we keep $\delta = \pi/2$, maneuvering in α from 0 to $\pi/4$ after, approximately, 1.9 adimensional time units.

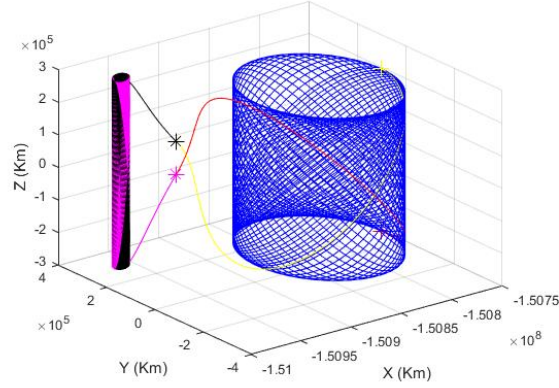


Figure 20: Connections towards the same final orbit changing only the initial value of the second phase: $\phi_2 = 0$ and $\phi_2 = \pi$.

4.3 Heteroclinic enhanced connections varying the clock angle for fixed ϕ_1 and ϕ_2

4.3.1 Evolution of the final unstable amplitude for clock angle maneuvers

In this section we study connections between Lissajous orbits by means of changing the clock angle δ for different fixed values of α_i . As in the preceding section, we keep fixed the value of the lightness number $\beta = 0.02$, and the size of the departing orbit, given by the amplitudes $A_x = 1/24$, and $A_z = 1/6$ in adimensional units.

Again, during the adimensional time interval $[0, 15]$ we explore the leg of the unstable manifold of the departing orbit taking $A_u = -10^{-4}$, $A_s = 0$, and starting phases at $t = 0$: $\phi_1 = \phi_2 = 0$. Along the states of this orbit we consider a potential change of the initial clock angle $\delta_i = \pi/2$ into a fixed final value $\delta_f \in (-\pi/2, 3\pi/2)$, so the maneuver is given by $\Delta\delta = \delta_f - \delta_i \in (-\pi, \pi)$. Then we compute the unstable component of the resulting state, associated to the new sail parameters, looking for the connection condition $A'_u = 0$. The resulting unstable amplitude curves $A'_u(t)$ depend on the value of α_i , and for $\alpha_i = -0.45$, -0.78 , $+0.78$ are given in Fig. 21.

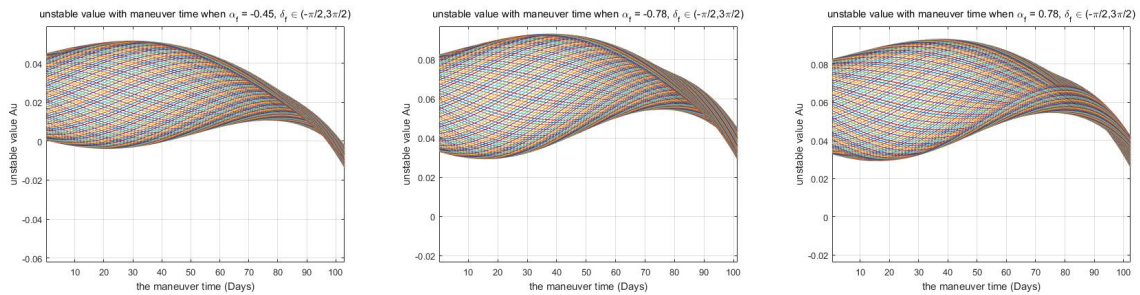


Figure 21: Behavior of A'_u vs maneuver time for $\alpha_f = -0.45, -0.78$ and 0.78 , and $\delta_f \in (-\pi/2, 3\pi/2)$.

Each curve in Fig. 21 corresponds to a different value of $\delta_f \in (-\pi/2, 3\pi/2)$. It follows that if $\alpha_i = -0.45$, there are three different behaviors, according to the number of crossings of the $A'_u = 0$ axis of the lines associated to different δ_f values. This number can be one if $\delta_f \in (-\pi/2, 0.91)$ and $\delta_f \in (2.33, 3\pi/2)$, two when $\delta_f \in (1.94, 2.19)$, or three when $\delta_f \in (0.92, 1.93)$ and $\delta_f \in (2.20, 2.34)$. For the other two values of α_i , there are no transfer possibilities, since there are no crossings with the $A'_u = 0$ line. Fig. 22 shows the three amplitude curves $A'_u(t)$ for $\delta_f = 0$ (only one $A'_u = 0$ crossing), $\delta_f = 1.6$ (three $A'_u = 0$ crossings), and $\delta_f = 2$ (two $A'_u = 0$ crossings), and Fig. 23 shows the initial, transfer and final orbits obtained for each case.

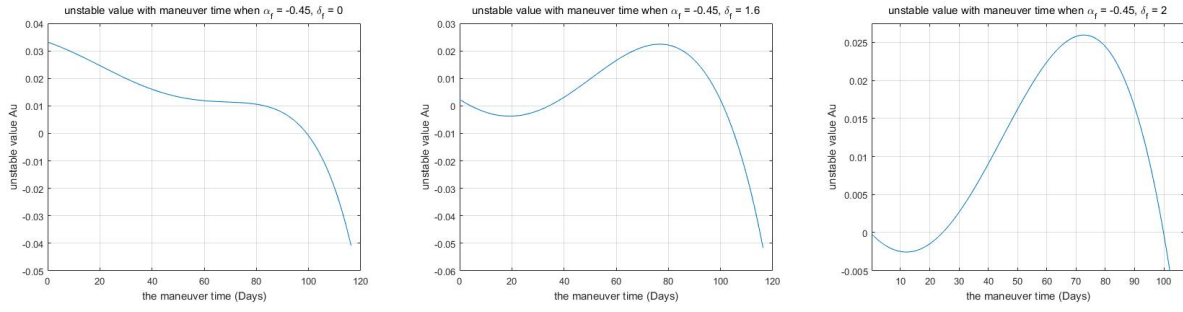


Figure 22: Behavior of the unstable amplitude curves $A'_u(t)$ for $\alpha_i = -0.45$, $\delta_i = \pi/2$, and different $\Delta\delta = \delta_f - \delta_i$ maneuvers.

Next we explore four different cases, according to the value of α_i , that, as we have seen can produce one, two, or three different connections. Fig. 24 shows the results obtained for $\alpha_i = \pi/4, -0.35, -0.45$, and $-\pi/4 = -0.7854$ (with $\Delta\alpha = \alpha_f - \alpha_i = 0$). For all the computations $\delta_i = \pi/2$ is fixed, and δ_f varies in $(-\pi/2, 3\pi/2)$.

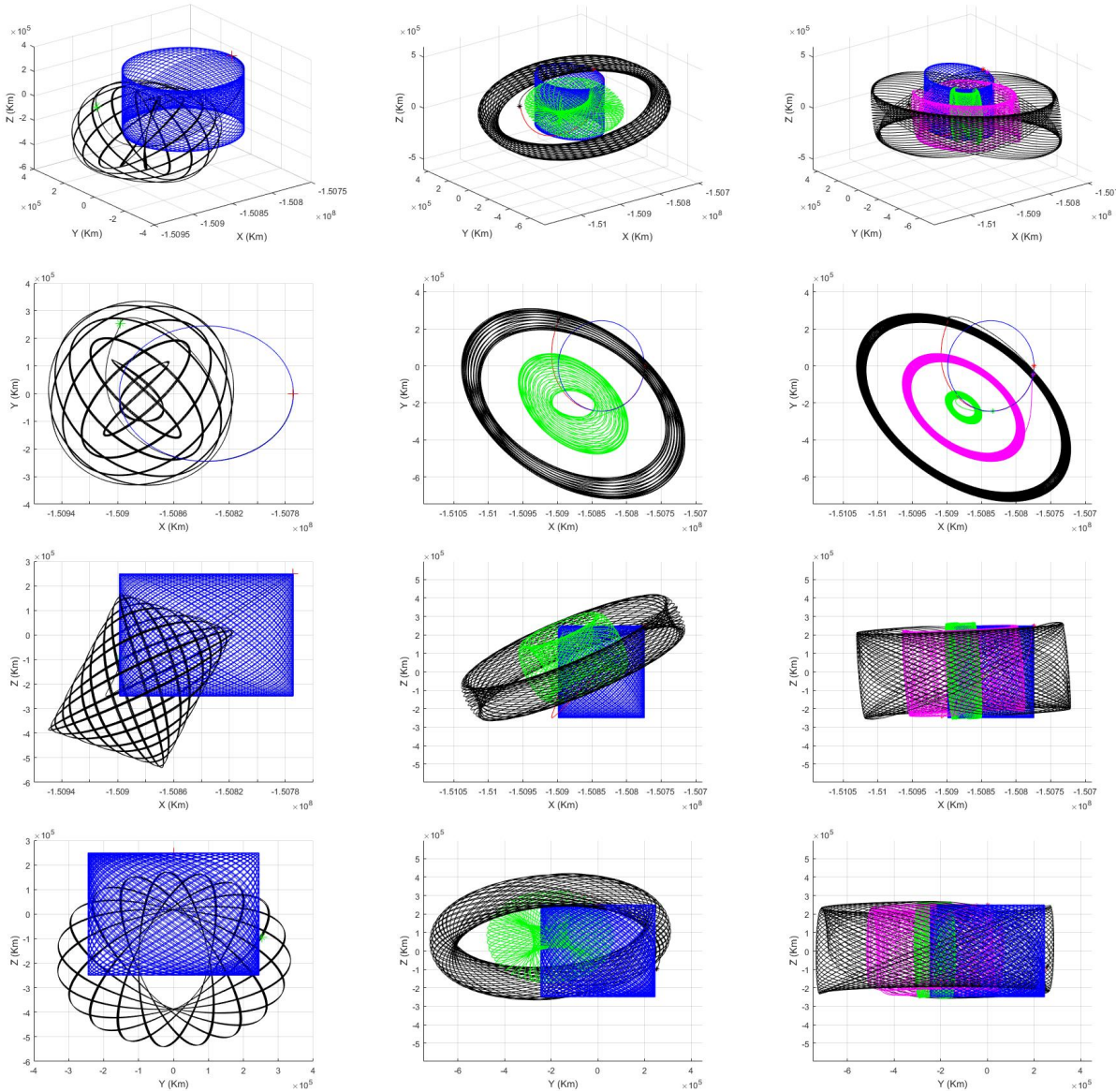


Figure 23: The left, central, and right columns correspond to $\delta_f = 0$ (one $A'_u = 0$ crossing), $\delta_f = 2$ (two $A'_u = 0$ crossings), and $\delta_f = 1.6$ (three $A'_u = 0$ crossings), respectively.

From the plots in the top and bottom rows of Fig. 24, corresponding to $\alpha_i = \pi/4$ and $\alpha_i = -\pi/4$, we can conclude that changing the δ_f value does not affect the number of crossing with the $A'_u = 0$ axis. The two middle rows, corresponding to $\alpha_i = -0.35$, and $\alpha_i = -0.45$, correspond to parameter values for which there are one, two or three transfer possibilities when $\delta_f \in (-\pi/2, 3\pi/2)$. Next we give some detailed results about these transitions when $\alpha_i = -0.45$, which are summarized in Table 3. This table shows the the values of the maneuver time and amplitudes of the Lissajous final orbits before and after the tangency.

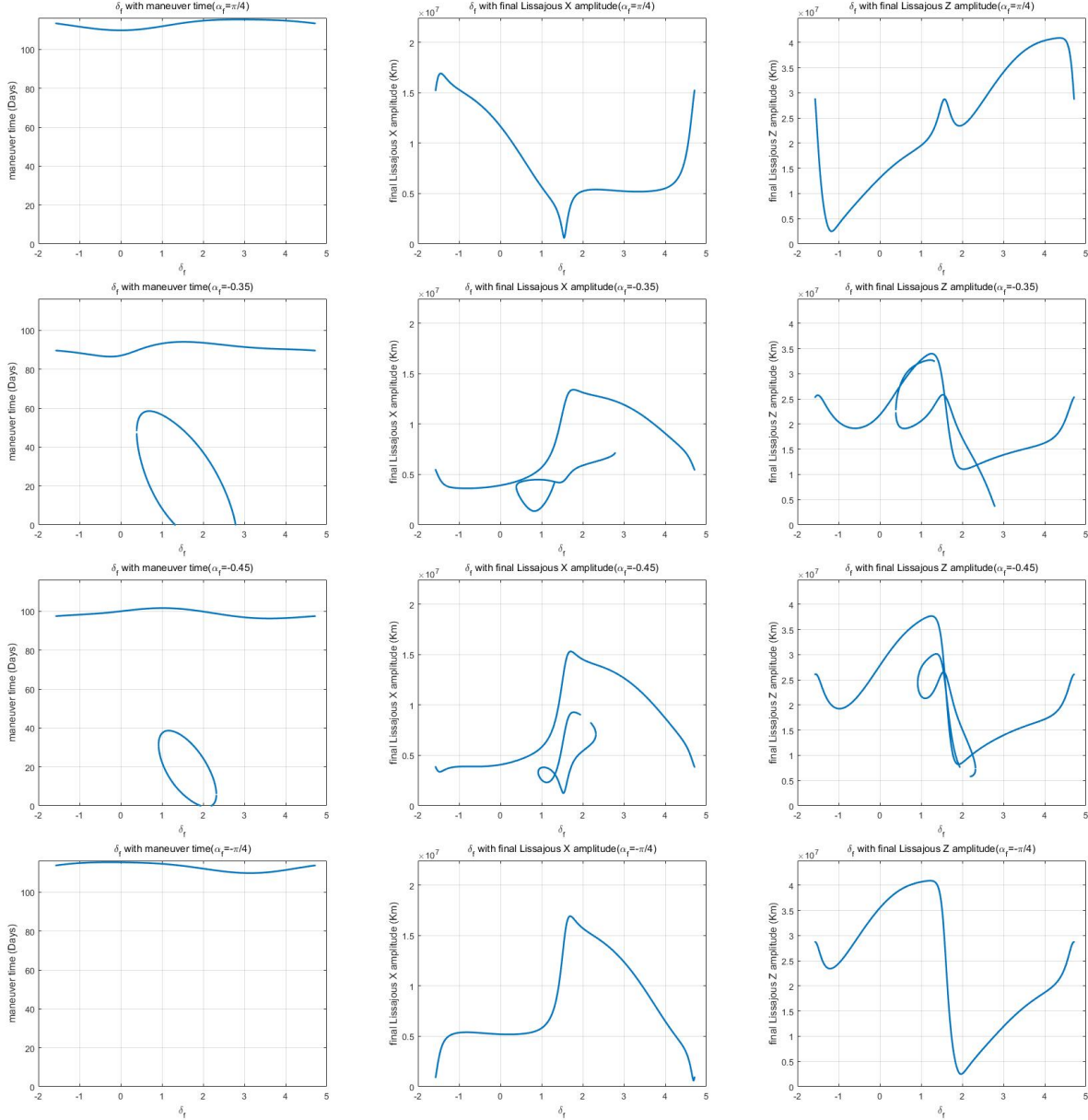


Figure 24: Behavior of the maneuver time, the A'_x , A'_z amplitudes as a function of δ maneuvers. The results correspond to $\alpha_f = \pi/4$, -0.35 , -0.45 and $-\pi/4$.

1. When δ_f varies between 0.91 and 0.92, the number of transfers goes from 1 to 3, since in this interval the curve $A'_u(\delta_f)$ goes through a tangency with the $A'_u = 0$ line for $\delta_f \approx 0.905$. Fig. 25 shows the behavior of A'_u as a function of the maneuver time for this value of δ_f .
2. When δ_f varies between 1.94 and 1.95, the number of transfers goes from 3 to 2, since in this interval the curve $A'_u(\delta_f)$ goes through a tangency with the $A'_u = 0$ line for $\delta_f \approx 1.94$.

3. When δ_f varies between 2.19 and 2.20, the number of transfers goes from 2 to 3, since in this interval the curve $A'_u(\delta_f)$ goes through a tangency with the $A'_u = 0$ line for $\delta_f \approx 2.20$.
4. When δ_f varies between 2.31 and 2.32, the number of transfers goes from 3 to 1, since in this interval the curve $A'_u(\alpha_f)$ goes through a tangency with the $A'_u = 0$ line for $\delta_f \approx 2.32$.

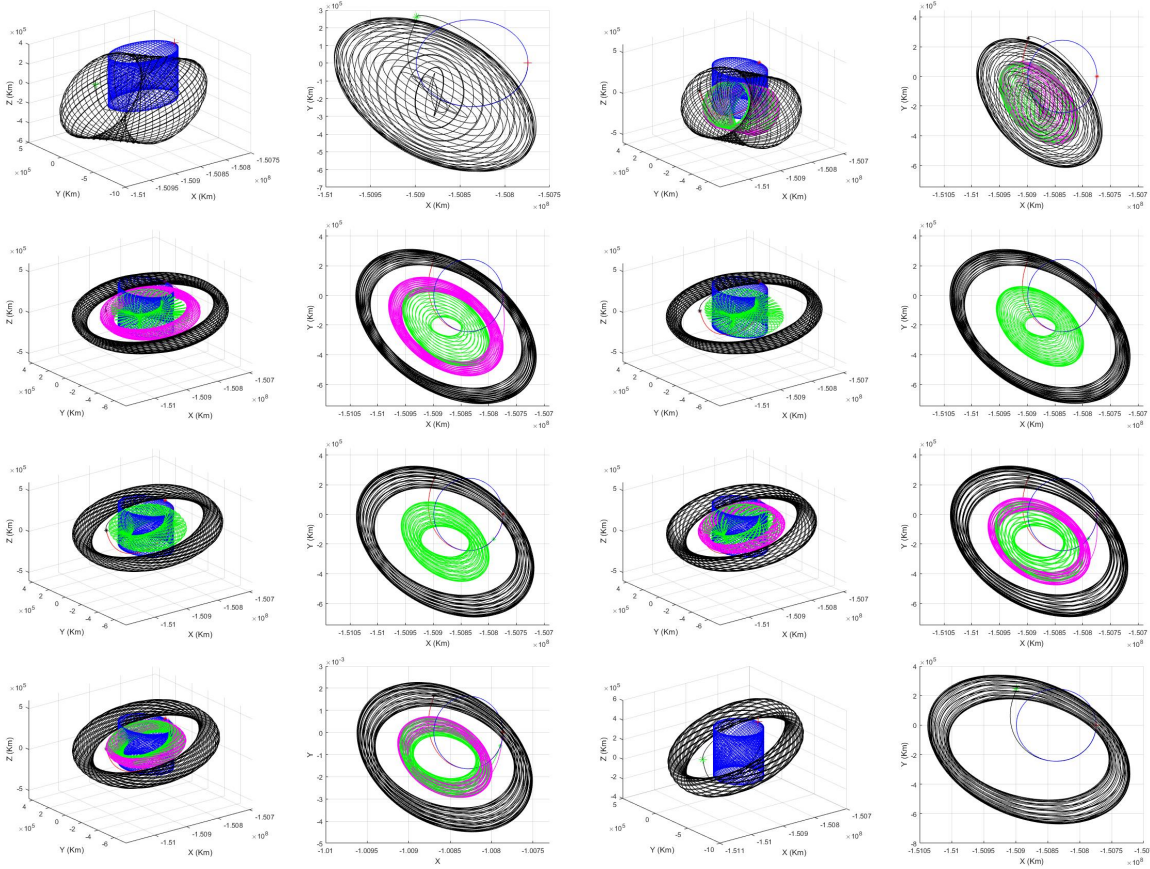


Figure 25: Departing (blue) and final Lissajous (green, magenta, and black) orbits.

Fig. 25 shows the departing (blue) and final Lissajous (green, magenta, and black) orbits, together with the transfer path that follows the unstable manifold of the departing orbit, until the maneuver time, and the stable manifold of the final one. The first row corresponds to the transition $\delta_f \in (0.91, 0.92)$, the second row corresponds to the transition $\delta_f \in (1.94, 1.95)$, the third row corresponds to the transition $\delta_f \in (2.19, 2.20)$, and fourth row corresponds to the transition $\delta_f \in (2.31, 2.32)$.

If we allow α_i to vary in $(-\pi/2, \pi/2)$ and $\delta_f \in (-\pi/2, 3\pi/2)$ while keeping $\delta_i = \pi/2$ and $\phi_1 = \phi_2 = 0$, Fig. 26 shows the values of the maneuver time and the X and Z amplitudes, when $\alpha_f \in (-\pi/2, \pi/2)$, $\delta_f \in (-\pi/2, 3\pi/2)$, and $\phi_1 = \phi_2 = 0$ in the top line. The bottom line shows the projection of the three surfaces on a coordinate plane: α_f -maneuver time, $\alpha_f - X$ amplitude, and $\alpha_f - Z$ amplitude.

In the preceding computations we have always set the value of the clock angle before the maneuver, δ_i , equal to $\pi/2$. When this angle changes the maneuver time also does.

Fig. 27 shows the values of the maneuver time and the X and Z amplitudes, when both the initial δ_i and final δ_f vary in $(-\pi/2, 3\pi/2)$, keeping fixed the values of the remaining parameters: $\alpha_i = 0$, $\alpha_f = -0.45$, $A_u = -10^{-4}$, $A_x = 1/24$, $A_z = 1/6$, and $\phi_1 = \phi_2 = 0$. The bottom line the figure shows the projection of the three surfaces on a coordinate plane: δ_f -maneuver time, δ_f - X amplitude, and δ_f - Z amplitude. Comparing the bottom line in Fig. 27 and Fig. 24, we can conclude that δ_i does not affect the maneuver time and the final X and Z amplitudes.

Table 3: Maneuver time and Lissajous final amplitudes of the transfers close to the tangencies with $A_u = 0$ for clock angle maneuvers.

Tangency transition	δ_f	Maneuver time (days)	Final X-amplitude A_x (10^6 km)	Final Z-amplitude A_z (10^6 km)
1 \rightarrow 3	0.91	101.7	5.42	36.37
	0.92	30.2	3.22	24.85
	0.92	32.5	3.43	23.92
	0.92	101.7	5.54	36.41
3 \rightarrow 2	1.94	0.0009	9.05	7.67
	1.94	26.3	5.22	16.37
	1.94	100.1	14.68	8.29
	1.95	26.0	5.27	16.16
	1.95	100.0	14.65	8.32
2 \rightarrow 3	2.19	68.1	7.48	24.95
	2.19	75.1	8.42	24.94
	2.20	0.003	8.21	5.83
	2.20	16.4	6.12	11.20
	2.20	99.2	14.17	9.92
3 \rightarrow 1	2.31	3.59	7.41	6.69
	2.31	8.4	6.81	8.20
	2.31	98.8	14.02	10.62
	2.32	98.8	14.00	10.68

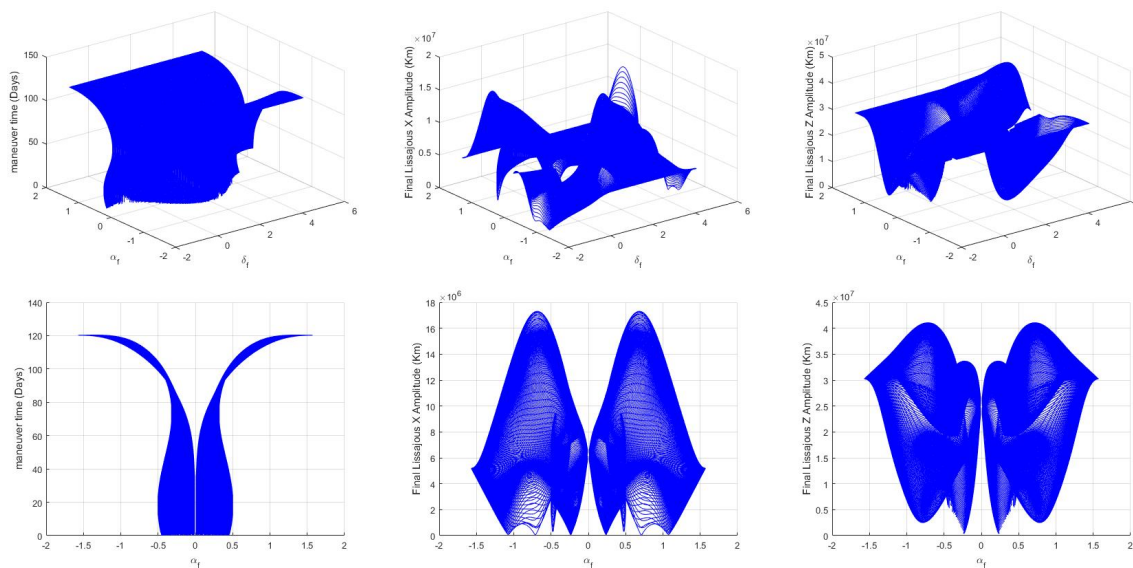


Figure 26: The values of the maneuver time and the X and Z amplitudes, when $\alpha_f \in (-\pi/2, \pi/2)$, $\delta_f \in (-\pi/2, 3\pi/2)$, and $\phi_1 = \phi_2 = 0$.

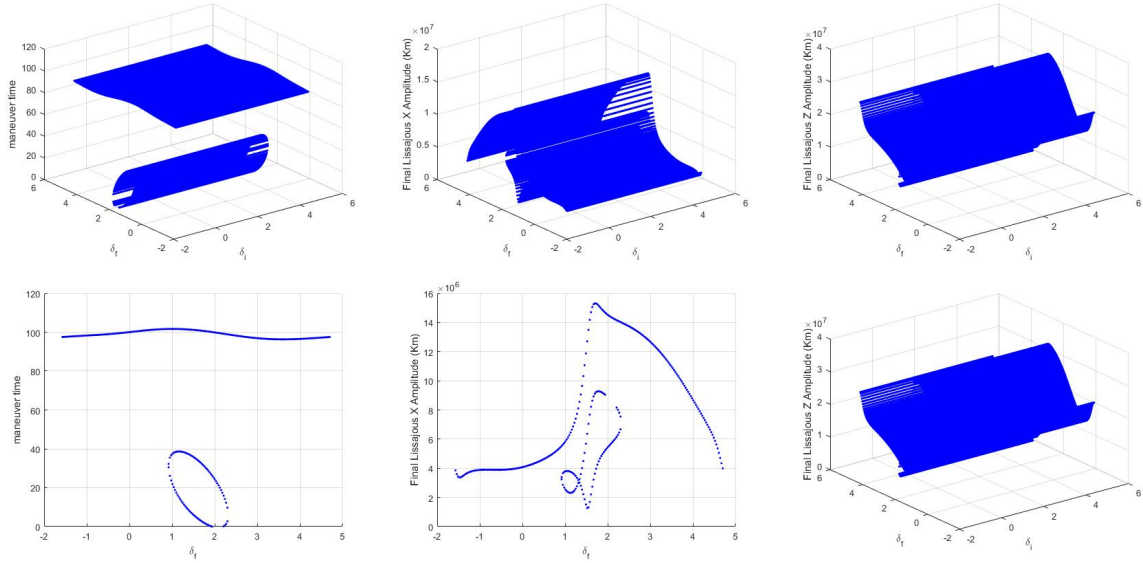


Figure 27: Maneuver times and final X and Z amplitudes, when $\alpha_f = -0.45$, $\delta_i \in (-\pi/2, 3\pi/2)$ and $\delta_f \in (-\pi/2, 3\pi/2)$.

4.4 Heteroclinic enhanced connections varying of the clock angle and phases ϕ_1 and ϕ_2

In the previous section we studied transfers associated to changes of the clock angle δ_f for fixed phases $\phi_1 = \phi_2 = 0$. Now we allow variations in both phases, which means that we consider different orbits of the unstable manifold of the departing Lissajous orbits.

As in the preceding section, for all the explorations that follow, we fix the initial and final values of the cone angle $\alpha_i = 0$, $\alpha_f = \pi/4$, as well as the size of the departing orbit, given by the amplitudes $A_x = 1/24$ and $A_z = 1/6$.

For the Fig. 28, In the first and third lines, values of the maneuver time and the X and Z amplitudes, when $\phi_1 \in (-\pi/2, 3\pi/2)$, $\phi_2 = 0$ (first line), and $\phi_1 = 0$, $\phi_2 \in (-\pi/2, 3\pi/2)$ (third line). In both cases $\delta_f \in (-\pi/2, 3\pi/2)$. The second and forth lines show the projection of the surfaces on the coordinate planes: δ_f -maneuver time, δ_f - X amplitude, and δ_f - Z amplitude, respectively.

4.5 Heteroclinic enhanced connections varying the cone angle for different values of the reflectivity parameter

In this section, we consider the influence of variations of the β parameter when it varies in $(0.01, 0.1)$. The initial and final cone and clock angles are: $\alpha_i = 0$, $\alpha_f = \pi/4$, $\delta_i = \delta_f = \pi/2$. As in the preceding sections, the amplitudes of the Lissajous orbit are: $A_x = 1/24$ and $A_z = 1/6$.

Fig. 29 shows the values of the maneuver time and the X and Z amplitudes, when $\beta_i = 0$ and $\beta_f \in (0.01, 0.1)$. The top line correspond to use as transfer orbit the one of the unstable manifold departing from $\phi_1 = \phi_2 = 0$, and the bottom line when $\phi_1 \in (-\pi/2, 3\pi/2)$, $\phi_2 \in (-\pi/2, 3\pi/2)$. Fig. 30 displays 3D representation and XY coordinate projection of two transfers performed changing the cone angle from $\alpha_i = 0$ to $\alpha_f = \pi/4$, for two different values of the β parameter. Both departing Lissajous orbits have the same amplitudes $A_u = -10^{-4}$, $A_s = 0$, $A_x = 1/24$, $A_z = 1/4$, but two different β values $\beta = 0.02$ (in blue), and $\beta = 0.1$ (in red).

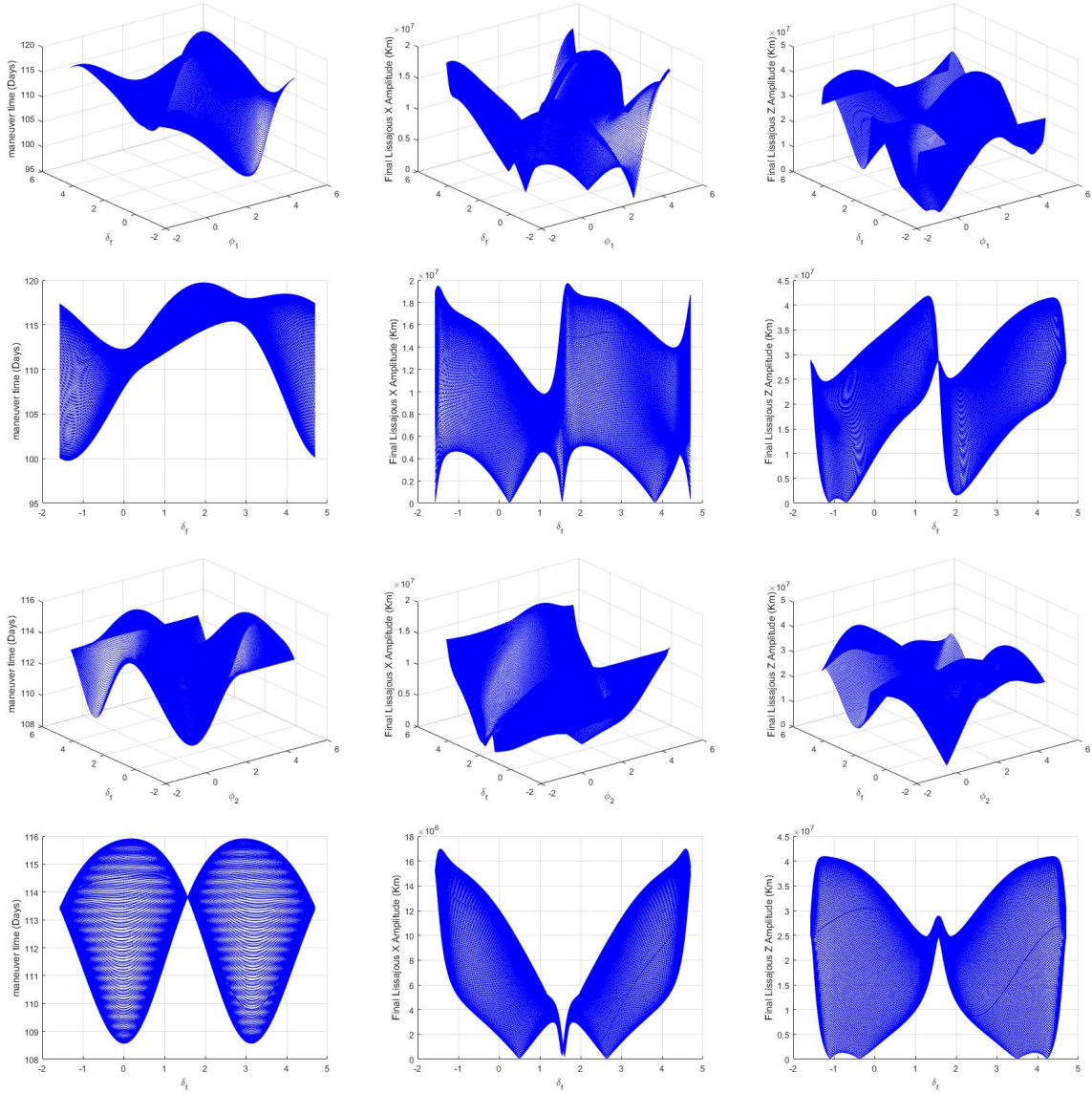


Figure 28: Values of the maneuver time and the final X and Z amplitudes, as function of ϕ_1 , ϕ_2 and δ_f .

5 Libration point exclusion zone avoidance

For orbits around L_1 in the Sun-Earth system there is region around the solar disk, as seen from the Earth, that has to be avoided in order that the data coming from the spacecraft be not hidden by the electromagnetic radiation of the Sun. This exclusion zone is, approximately, of three degrees about the solar disc as seen from the Earth. Something similar happens for orbits around the L_2 point of the same system, where the spacecraft must avoid the regions eclipsed by the Earth or, eventually, some bright regions of the sky. In most of these cases the exclusion zone is a disk in the y - z plane centered along the x -axis. This is the situation considered in this paper, so the exclusion zone, in the configuration space, is defined by

$$y^2 + z^2 < R^2,$$

with $R = 90\,000$ km (see [26] and references herein).

Figure 31 shows the 3-D view of two exclusion disks of a Lissajous orbit (left) around the Sun-Earth L_2 point with $A_x = 1/24$ and $A_z = 1/6$, and its representation using the EPP (right). In this example the disks represent the eclipsed regions by the Earth. The value of the two frequencies ω_1 and ω_2 associated to this orbit are $\omega_1 = 2.571904$ and $\omega_2 = 2.51130744$, so the slope of the lines in the EPP representation of the Lissajous orbit is $\omega_2/\omega_1 = 0.976439019$. If the length of the mission in a Lissajous orbit is long enough, since the slope of the orbits in the EPP (ω_2/ω_1) is close to one, the satellite will irremediably cross the exclusion zone, so some maneuvers must be foreseen to avoid it.

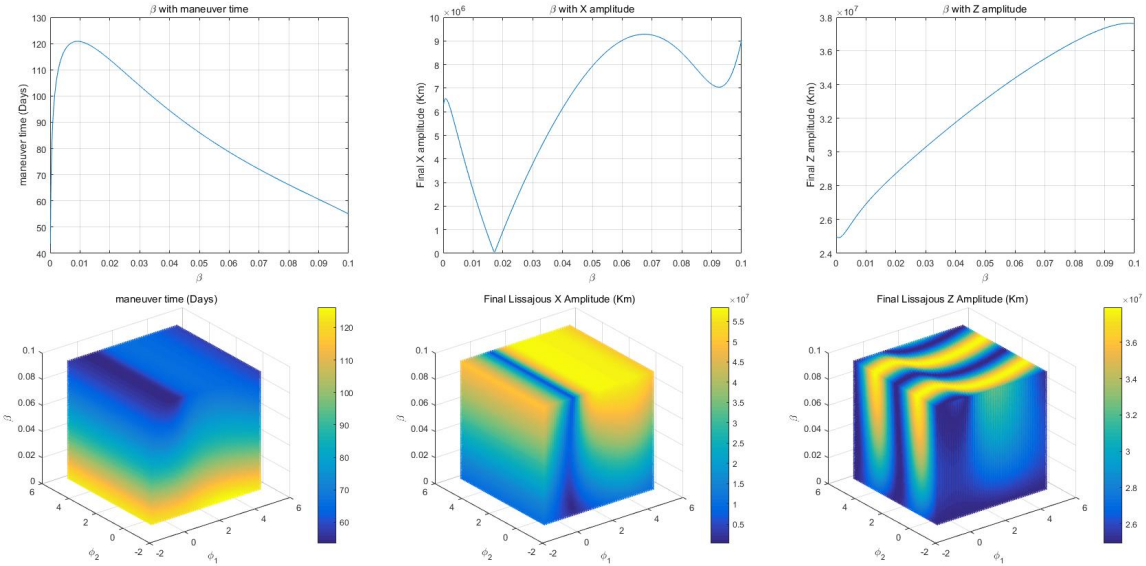


Figure 29: Maneuver times and final X and Z amplitudes, when $\beta_i = 0$ and $\beta_f \in (0.01, 0.1)$.

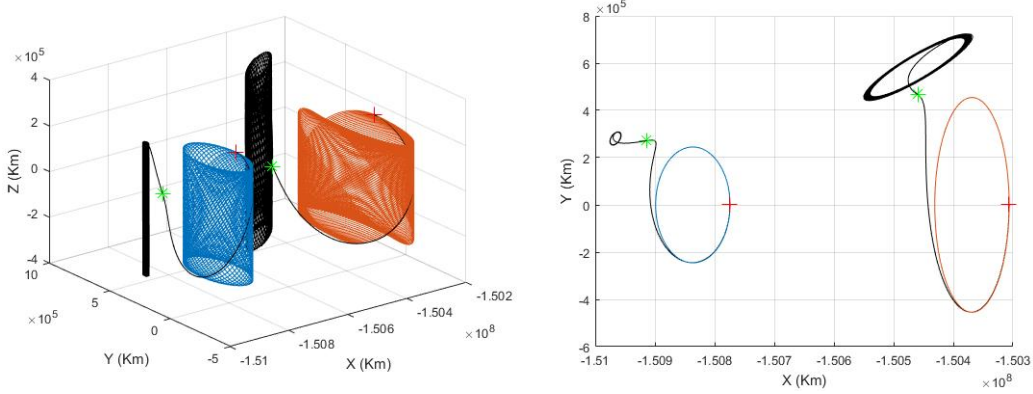


Figure 30: 3D representation and XY coordinate projection for two different values of the β parameter.

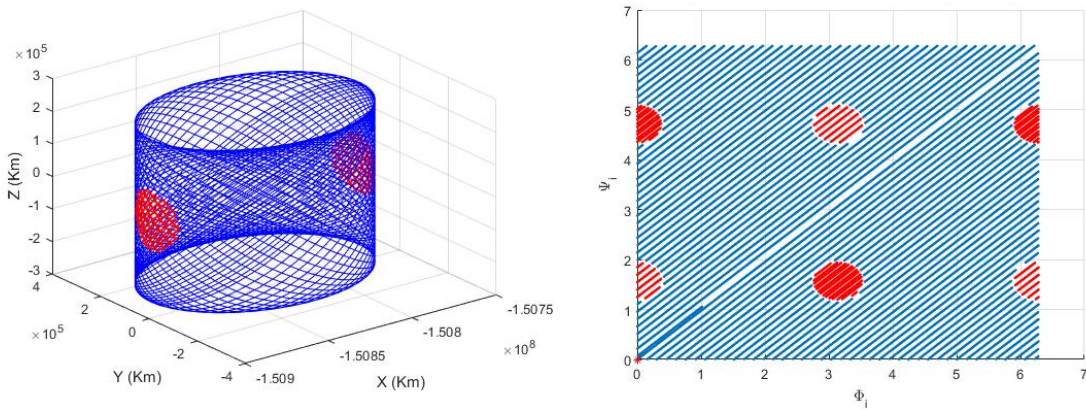


Figure 31: 3-D view of two exclusion disks of a Lissajous orbit (left) and its representation using the EPP (right). More details about this representation can be found in [26].

When the solar sail parameters vary the equilibrium points also do, so, in many cases they are no longer aligned with the Sun-Earth direction. As a consequence, after a solar sail maneuver the exclusion zone of the Lissajous orbit changes and, eventually, it can disappear. As an example, consider a transfer maneuver, departing from the Lissajous orbit with $A_x = 1/24$ and $A_z = 1/6$, associated to a change of the cone angle from $\alpha_i = 0$ to $\alpha_f = -0.45$, with the

value of the clock angle fixed to $\delta = \pi/2$. Fig. 32 shows the value of the maneuver time as function of $\phi_1 \in (-\pi, \pi)$. Recall that in this case the value of ϕ_2 does not affect the maneuver time and amplitude of the final Lissajous orbit.

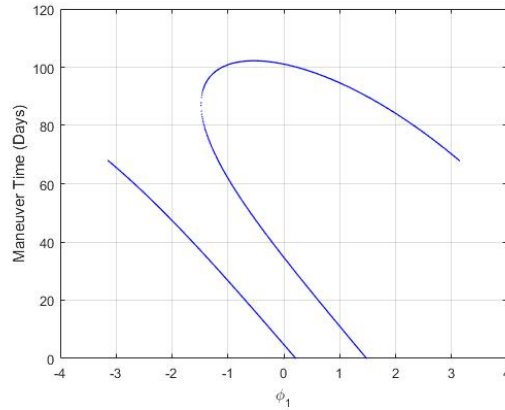


Figure 32: Possible maneuver times as a function of $\phi_1 \in (-\pi, \pi)$.

From Fig. 32 it follows that, depending on the value of ϕ_1 there is one $\phi_1 \in (-\pi, -1.48)$ and $\in (1.48, \pi)$, two $\phi_1 \in (0.21, 1.48)$ or three $\phi_1 \in (-1.48, 0.21)$ transfer possibilities. For $\phi_1 = 0, \phi_2 = 0$, Fig. 33 shows the $x-y$ projection and EPP representation of the departing and arrival Lissajous orbits associated to a connection accomplished with just a variation of the cone angle from $\alpha_i = 0$ to $\alpha_f = -0.45$. The departing point of the unstable manifold corresponding to $\phi_1 = 0, \phi_2 = 0$ allows three connections at three different epochs, as is shown in Fig. 32. With the first maneuver, the exclusion zone is reached after 105.8 days, and with the third after 935.3 days. Note that with the second maneuver the exclusion zone disappeared. Two dashed parallel lines in the upper left plot represent the exclusion zone. As is clear from the plots, in some cases the forbidden zone of the target orbit is larger than the one of the departing Lissajous, in other cases, because the libration point has moved and the target orbit has reduced its amplitude, the forbidden zone disappears.

As we have already said, for any transfer the variation of the value of ϕ_2 does not change either the target orbit and the maneuver time, but it changes the orbit of the unstable manifold used for the connection. This means that it may happen that once the final orbit is reached, it can take a long time before the exclusion zone is reached. This is what is shown in Fig. 35, the EPP representation of the departing and arrival Lissajous orbits and exclusion zones associated to connections performed just with a variation of the cone angle from $\alpha_i = 0$ to $\alpha_f = -0.45$. The departing point of the unstable manifold corresponds to $\phi_1 = 0$ and, from top to bottom, $\phi_2 = \pi/4, \pi/2, \pi, 3\pi/2$ and $7\pi/4$.

In the Fig. 34, we show an example of an exclusion zone avoidance maneuver with the parameters: $\alpha_i = 0, \alpha_f = -0.45, \delta_i = \delta_f = \pi/2, \phi_1 = 0, \phi_2 = 1$. The left figure shows the trajectory from the initial Lissajous orbits (in blue) to the final Lissajous orbits (in black), the red arcs represent exclusion zones. The right figure is the associated EPP representation. The departure is at the point with coordinates (0,1) in the y-axis, which moves along the lines with slope $\omega_2/\omega_1 = 0.976$ until it reaches a blue region, which are the exclusion zones; then cone angle is changed to $\alpha_f = -0.45$, that corresponds to a jump in the EPP, and the new exclusion zones are the red ones. The new orbit needs about 861 days to reach (tangently) the red area.

6 Conclusion

This paper investigates heteroclinic enhanced connections between libration point orbits using solar sailing. They can be seen as transfer trajectories continuous in both position and velocity in a changing vectorfield, with many potential applications including libration point exclusion avoidance. The dynamical model considered is the CR3BP including the solar radiation pressure, and the key point for the analysis is the representation of the solutions of the linearized system about the artificial equilibrium points, that change position according to the sail attitude and its reflective properties.

The invariant manifolds of libration point orbits are considered for the obtaintion of transfer trajectories joining Lissajous orbits in the Sun-Earth system, and the transfer maneuvers are performed by changing the angular parameters;

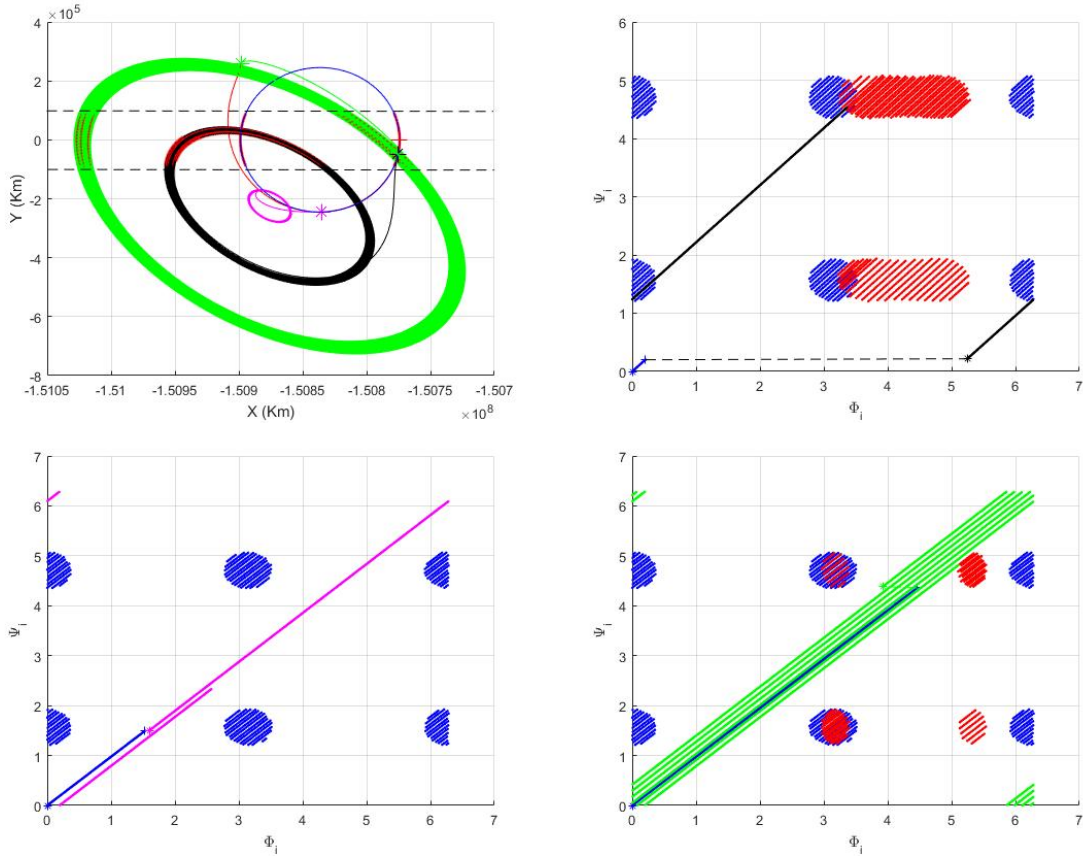


Figure 33: $x - y$ projection and EPP representation of the departing and arrival Lissajous orbits associated to a connection obtained just changing the cone angle from $\alpha_i = 0$ to $\alpha_f = -0.45$ at three different epochs, in order to avoid the exclusion zone. Exclusion zones of the departure Lissajous are plotted in blue while the ones of the arrival orbit are in red.

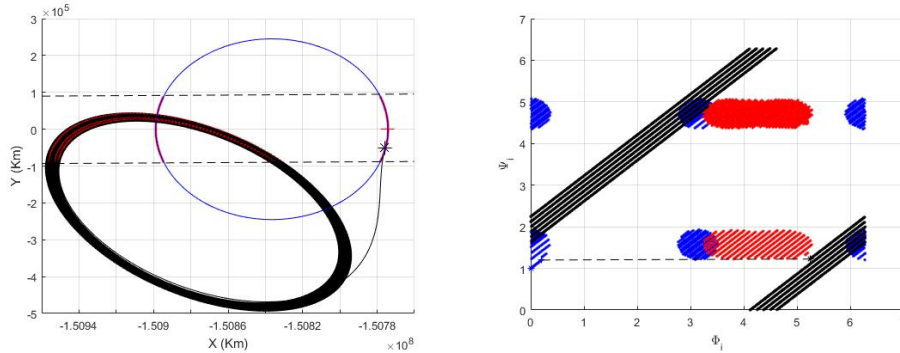


Figure 34: An example of an exclusion zone avoidance maneuver.

the so called cone and clock angles, that determine the orientation of the sail with respect to the Sun, as well as phases, reflectivity parameter and initial amplitudes.

The connections considered correspond to:

1. Select one orbit of the unstable manifold of the departing Lissajous orbit, and to explore the different transfer possibilities associated to transfer maneuvers done by means of cone and clock angle variations and, for a fixed cone (or clock) angle variation, to different epochs at which the solar-sail maneuver is performed.
2. Consider all the orbits of the unstable manifold of the departing Lissajous orbit, and to explore the different connection possibilities associated to the cone and clock angles solar-sail maneuvers departing from a fixed cone

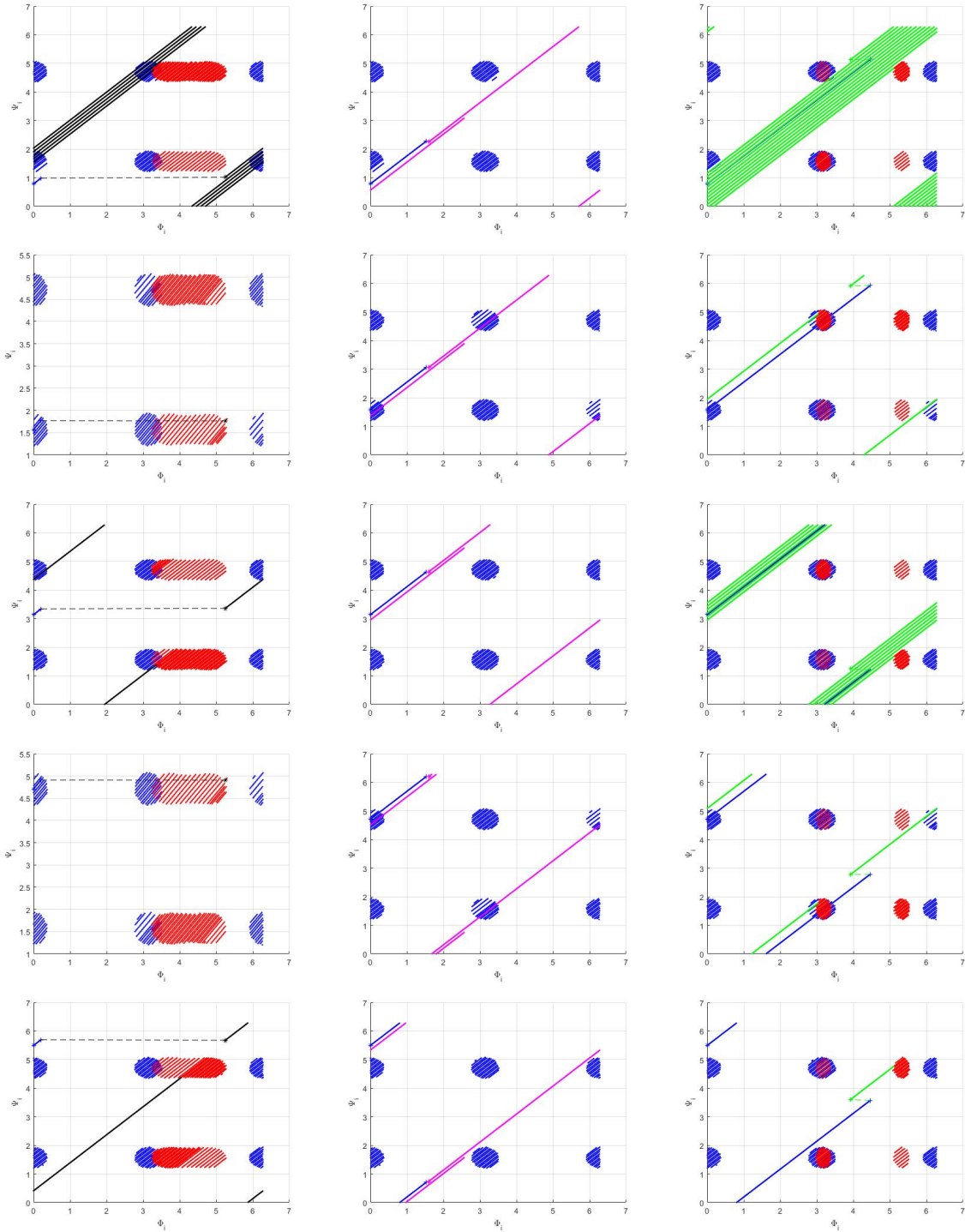


Figure 35: EPP representation of the departing and arrival Lissajous orbits.

angle value.

3. Apart from the above parameters, the paper considers the reflectivity parameter β and initial X and Z amplitudes (A_{xi}, A_{zi}) that impact the solar-sail maneuvers and final Lissajous orbits amplitude.

In all cases the results obtained include a description of the size of the final Lissajous orbit together with the epoch at which the solar-sail maneuver has to be performed (i.e. the transfer time).

Appendix A

Values of the coefficients a_i , b_i , and c_i , for $i = 0, \dots, 3$, that appear in the linearized equations of motion (2). It must be noted that the values of a_0 , b_0 and c_0 are zero at the equilibrium points, so they do not appear in the differential equations.

$$\begin{aligned}
a_0 &= -A_1 \mp \frac{\mu}{\gamma} + \frac{1-\mu}{\gamma^3} \frac{A_1}{D_1^3} + \frac{\mu}{\gamma^3} \frac{A_2}{D_2^3} - \frac{\beta(1-\mu)\cos^2\alpha}{\gamma^3 D_1^3 D_3} (A_1 D_3 \cos\alpha + C_1 A_1 \sin\alpha \cos\delta + B_1 D_1 \sin\alpha \sin\delta), \\
a_1 &= 1 + \frac{1-\mu}{\gamma^3} \frac{3A_1^2 - D_1^2}{D_1^5} + \frac{\mu}{\gamma^3} \frac{3A_2^2 - D_2^2}{D_2^5} - \frac{\beta(1-\mu)\cos^2\alpha}{\gamma^3 D_1^3 D_3} \left(\frac{(3A_1^2 - D_1^2)D_3}{D_1^2} \cos\alpha \right. \\
&\quad \left. + C_1(E_3 A_1^2 - 1) \sin\alpha \cos\delta + B_1 E_2 A_1 D_1 \sin\alpha \sin\delta \right), \\
a_2 &= \frac{1-\mu}{\gamma^3} \frac{3A_1 B_1}{D_1^5} + \frac{\mu}{\gamma^3} \frac{3A_2 B_2}{D_2^5} - \frac{\beta(1-\mu)\cos^2\alpha}{\gamma^3 D_1^3 D_3} \left(\frac{3A_1 B_1 D_3}{D_1^2} \cos\alpha + E_3 B_1 A_1 C_1 \sin\alpha \cos\delta \right. \\
&\quad \left. + (E_2 B_1^2 - 1) D_1 \sin\alpha \sin\delta \right), \\
a_3 &= \frac{1-\mu}{\gamma^3} \frac{3A_1 C_1}{D_1^5} + \frac{\mu}{\gamma^3} \frac{3A_2 C_2}{D_2^5} - \frac{\beta(1-\mu)\cos^2\alpha}{\gamma^3 D_1^3 D_3} \left(\frac{3A_1 C_1 D_3}{D_1^2} \cos\alpha + A_1 \left(\frac{3C_1^2}{D_1^2} - 1 \right) \sin\alpha \cos\delta + \frac{2B_1 C_1}{D_1} \sin\alpha \sin\delta \right), \\
b_0 &= -B_1 + \frac{1-\mu}{\gamma^3} \frac{B_1}{D_1^3} + \frac{\mu}{\gamma^3} \frac{B_2}{D_2^3} - \frac{\beta(1-\mu)\cos^2\alpha}{\gamma^3 D_1^3 D_3} (B_1 D_3 \cos\alpha + C_1 B_1 \sin\alpha \cos\delta - A_1 D_1 \sin\alpha \sin\delta), \\
b_1 &= \frac{1-\mu}{\gamma^3} \frac{3A_1 B_1}{D_1^5} + \frac{\mu}{\gamma^3} \frac{3A_2 B_2}{D_2^5} - \frac{\beta(1-\mu)\cos^2\alpha}{\gamma^3 D_1^3 D_3} \left(\frac{3A_1 B_1 D_3}{D_1^2} \cos\alpha + E_3 B_1 A_1 C_1 \sin\alpha \cos\delta \right. \\
&\quad \left. - (E_2 A_1^2 - 1) D_1 \sin\alpha \sin\delta \right), \\
b_2 &= 1 + \frac{1-\mu}{\gamma^3} \frac{3B_1^2 - D_1^2}{D_1^5} + \frac{\mu}{\gamma^3} \frac{3B_2^2 - D_2^2}{D_2^5} - \frac{\beta(1-\mu)\cos^2\alpha}{\gamma^3 D_1^3 D_3} \left(\frac{(3B_1^2 - D_1^2)D_3}{D_1^2} \cos\alpha \right. \\
&\quad \left. + C_1(E_3 B_1^2 - 1) \sin\alpha \cos\delta - B_1 E_2 A_1 D_1 \sin\alpha \sin\delta \right), \\
b_3 &= \frac{1-\mu}{\gamma^3} \frac{3B_1 C_1}{D_1^5} + \frac{\mu}{\gamma^3} \frac{3B_2 C_2}{D_2^5} - \frac{\beta(1-\mu)\cos^2\alpha}{\gamma^3 D_1^3 D_3} \left(\frac{3B_1 C_1 D_3}{D_1^2} \cos\alpha + B_1 \left(\frac{3C_1^2}{D_1^2} - 1 \right) \sin\alpha \cos\delta - \frac{2A_1 C_1}{D_1} \sin\alpha \sin\delta \right), \\
c_0 &= \frac{1-\mu}{\gamma^3} \frac{C_1}{D_1^3} + \frac{\mu}{\gamma^3} \frac{C_2}{D_2^3} - \frac{\beta(1-\mu)\cos^2\alpha}{\gamma^3 D_1^3 D_3} (C_1 D_3 \cos\alpha - D_3^2 \sin\alpha \cos\delta), \\
c_1 &= \frac{1-\mu}{\gamma^3} \frac{3A_1 C_1}{D_1^5} + \frac{\mu}{\gamma^3} \frac{3A_2 C_2}{D_2^5} - \frac{\beta(1-\mu)\cos^2\alpha}{\gamma^3 D_1^3 D_3} \left(\frac{3A_1 C_1 D_3}{D_1^2} \cos\alpha - (E_3 D_3^2 - 2) A_1 \sin\alpha \cos\delta \right), \\
c_2 &= \frac{1-\mu}{\gamma^3} \frac{3C_1 B_1}{D_1^5} + \frac{\mu}{\gamma^3} \frac{3B_2 C_2}{D_2^5} - \frac{\beta(1-\mu)\cos^2\alpha}{\gamma^3 D_1^3 D_3} \left(\frac{3B_1 C_1 D_3}{D_1^2} \cos\alpha - (E_3 D_3^2 - 2) B_1 \sin\alpha \cos\delta \right), \\
c_3 &= \frac{1-\mu}{\gamma^3} \left(\frac{3C_1^2 - D_1^2}{D_1^5} \right) + \frac{\mu}{\gamma^3} \left(\frac{3C_2^2 - D_2^2}{D_2^5} \right) - \frac{\beta(1-\mu)\cos^2\alpha}{\gamma^3 D_1^3 D_3} \left(\frac{(3C_1^2 - D_1^2)D_3}{D_1^2} \cos\alpha - \frac{3C_1}{D_1^2} D_3^2 \sin\alpha \cos\delta \right),
\end{aligned}$$

where

$$\begin{aligned}
A_1 &= A_3 = \frac{\gamma_1 - \mu}{\gamma}, & A_2 &= \frac{\gamma_1 - \mu + 1}{\gamma}, \\
B_1 &= B_2 = B_3 = \frac{\gamma_2}{\gamma}, \\
C_1 &= C_2 = -\frac{\gamma_3}{\gamma}, & C_3 &= 0, \\
D_i^2 &= A_i^2 + B_i^2 + C_i^2, & \text{for } i &= 1, 2, 3 \\
E_1 &= \frac{D_1^2 + D_3^2}{D_1^2 D_3^2}, & E_2 &= \frac{D_1^2 + 2D_3^2}{D_1^2 D_3^2}, & E_3 &= \frac{D_1^2 + 3D_3^2}{D_1^2 D_3^2}.
\end{aligned}$$

Appendix B

Values of the coefficients k_i and \bar{k}_i , for $i = 1, \dots, 6$, that appear in the final form of the solution (8).

$$k_i = \frac{\lambda_i^4 - (c_3 + a_1)\lambda_i^2 + a_1c_3 - a_3c_1}{2\lambda_i^3 + a_2\lambda_i^2 - 2c_3\lambda_i - a_2c_3 + a_3c_2}, \quad \text{for } i = 1, 2,$$

$$\begin{aligned} k_3 &= \frac{AC + BD}{C^2 + D^2}, & k_4 &= \frac{AD - BC}{C^2 + D^2}, \\ k_5 &= \frac{EG + FH}{G^2 + H^2}, & k_6 &= -\frac{FG - EH}{G^2 + H^2}, \end{aligned}$$

$$\bar{k}_i = \frac{c_2\lambda_i^4 + 2c_1\lambda_i^3 + (a_2c_1 - c_2c_3 - a_1c_2)\lambda_i^2 - 2c_1c_3\lambda_i + a_1c_2c_3 - a_2c_1c_3}{2\lambda_i^5 + a_2\lambda_i^4 - 4c_3\lambda_i^3 + (a_3c_2 - 2a_2c_3)\lambda_i^2 + 2c_3^2\lambda_i + a_2c_3^2 - a_3c_2c_3}, \quad \text{for } i = 1, 2,$$

$$\begin{aligned} \bar{k}_3 &= \frac{\bar{A}\bar{C} + \bar{B}\bar{D}}{\bar{C}^2 + \bar{D}^2}, & \bar{k}_4 &= \frac{\bar{A}\bar{D} - \bar{B}\bar{C}}{\bar{C}^2 + \bar{D}^2}, \\ \bar{k}_5 &= \frac{\bar{H}\bar{F} + \bar{E}\bar{G}}{\bar{G}^2 + \bar{H}^2}, & \bar{k}_6 &= -\frac{\bar{E}\bar{H} - \bar{F}\bar{G}}{\bar{G}^2 + \bar{H}^2}. \end{aligned}$$

where

$$\begin{aligned} A &= 4c_2\eta_1^3\omega_1 + (6c_1 - 4c_2)\eta_1\omega_1^3 - 2c_1\omega_1^3 - (2a_1c_2 - 2a_2c_1 + 2c_2c_3)\eta_1\omega_1 - 2c_1c_3\omega_1, \\ B &= c_2\eta_1^4 - 6c_2\eta_1^2\omega_1^2 + c_2\omega_1^4 + 2c_1\eta_1^3 - 6c_1\eta_1\omega_1^2 - (a_1c_2 - a_2c_1 + c_2c_3)\eta_1^2 + (a_1c_2 - a_2c_1 + c_2c_3)\omega_1^2 \\ &\quad - 2c_1c_3\eta_1 + a_1c_2c_3 - a_2c_1c_3, \\ C &= 10\eta_1^4\omega_1 - 20\eta_1^3\omega_1^2 + 2\omega_1^5 + 4a_2\eta_1^3\omega_1 - 4a_2\eta_1\omega_1^3 - 12c_3\eta_1^2\omega_1 + 4c_3\omega_1^3 - (4a_2c_3 - 2a_2c_3)\eta_1\omega_1 + 2c_3^2\omega_1, \\ D &= 2\eta_1^5 - 20\eta_1^3\omega_1^2 + 10\eta_1\omega_1^4 + a_2\eta_1^4 - 6a_2\eta_1^2\omega_1^2 + a_2\omega_1^4 + 12c_3\eta_1\omega_1^2 - (4c_3 + 2a_2c_3 - a_3c_2)\eta_1^2 \\ &\quad + (2a_2c_3 - a_3c_2)\omega_1^2 + 2c_3^2\eta_1 + a_2c_3^2 - a_3c_2c_3, \\ E &= 4\eta_2^3\omega_2 - 4\eta_2\omega_2^3 - (2a_1 + 2c_3)\eta_2\omega_2, \\ F &= \eta_2^4 - 6\eta_2^2\omega_2^2 + \omega_2^4 - (a_1 + c_3)\eta_2^2 + (a_1 + c_3)\omega_2^2 + a_1c_3 - a_3c_1, \\ G &= 2c_2\eta_2\omega_2 + 2c_1\omega_2, \\ H &= c_2\eta_2^2 - c_2\omega_2^2 + 2c_1\eta_2 - a_1c_2 + a_2c_1, \\ \bar{A} &= -4c_2\eta_1^3\omega_1 + (4c_2 - 6c_1)\eta_1\omega_1^3 - 2c_1\omega_1^3 + (2a_1c_2 - 2a_2c_1 + 2c_2c_3)\eta_1\omega_1 + 2c_1c_3\omega_1, \\ \bar{B} &= c_2\eta_1^4 - 6c_2\eta_1^2\omega_1^2 + c_2\omega_1^4 + 2c_1\eta_1^3 - 6c_1\eta_1\omega_1^2 - (a_1c_2 - a_2c_1 + c_2c_3)\eta_1^2 + (a_1c_2a_2c_1 + c_2c_3)\omega_1^2 \\ &\quad - 2c_1c_3\eta_1 + a_1c_2c_3 - a_2c_1c_3, \\ \bar{C} &= 10\eta_1^4\omega_1 - 20\eta_1^3\omega_1^2 + 2\omega_1^5 + 4a_2\eta_1^3\omega_1 - 4a_2\eta_1\omega_1^3 - 12c_3\eta_1^2\omega_1 + 4c_3\omega_1^3 - (4a_2c_3 - 2a_2c_3)\eta_1\omega_1 + 2c_3^2\omega_1, \\ \bar{D} &= 2\eta_1^5 - 20\eta_1^3\omega_1^2 + 10\eta_1\omega_1^4 + a_2\eta_1^4 - 6a_2\eta_1^2\omega_1^2 + a_2\omega_1^4 + 12c_3\eta_1\omega_1^2 - (4c_3 + 2a_2c_3 - a_3c_2)\eta_1^2 \\ &\quad + (2a_2c_3 - a_3c_2)\omega_1^2 + 2c_3^2\eta_1 + a_2c_3^2 - a_3c_2c_3, \\ \bar{E} &= 6\eta_2^2\omega_2 - 2\omega_2^3 + 2a_2\eta_2\omega_2 - 2c_3\omega_2, \\ \bar{F} &= 2\eta_2^3 - 6\eta_2\omega_2^2 + a_2\eta_2^2 - a_2\omega_2^2 - 2c_3\eta_2 - a_2c_3 + a_3c_2, \\ \bar{G} &= 2c_2\eta_2\omega_2 + 2c_1\omega_2, \\ \bar{H} &= c_2\eta_2^2 - c_2\omega_2^2 + 2c_1\eta_2 - a_1c_2 + a_2c_1. \end{aligned}$$

Appendix C

Components of the matrix $H = (h_{ij})$ appearing in the transformation (9).

$$\begin{aligned}
h_{11} &= e^{\lambda_1 t}, \\
h_{12} &= e^{\lambda_2 t}, \\
h_{13} &= e^{\eta_1 t} \cos \omega_1 t, \\
h_{14} &= e^{\eta_1 t} \sin \omega_1 t, \\
h_{15} &= e^{\eta_2 t} (\bar{k}_5 \cos \omega_2 t + \bar{k}_6 \sin \omega_2 t), \\
h_{16} &= e^{\eta_2 t} (\bar{k}_5 \sin \omega_2 t - \bar{k}_6 \cos \omega_2 t), \\
h_{21} &= k_1 e^{\lambda_1 t}, \\
h_{22} &= k_2 e^{\lambda_2 t}, \\
h_{23} &= e^{\eta_1 t} (k_3 \cos \omega_1 t + k_4 \sin \omega_1 t), \\
h_{24} &= e^{\eta_1 t} (k_3 \sin \omega_1 t - k_4 \cos \omega_1 t), \\
h_{25} &= e^{\eta_2 t} (k_5 \cos \omega_2 t + k_6 \sin \omega_2 t), \\
h_{26} &= e^{\eta_2 t} (k_5 \sin \omega_2 t - k_6 \cos \omega_2 t), \\
h_{31} &= \bar{k}_1 e^{\lambda_1 t}, \\
h_{32} &= \bar{k}_2 e^{\lambda_2 t}, \\
h_{33} &= e^{\eta_1 t} (\bar{k}_3 \cos \omega_1 t + \bar{k}_4 \sin \omega_1 t), \\
h_{34} &= e^{\eta_1 t} (\bar{k}_3 \sin \omega_1 t - \bar{k}_4 \cos \omega_1 t), \\
h_{35} &= e^{\eta_2 t} \cos \omega_2 t, \\
h_{36} &= e^{\eta_2 t} \sin \omega_2 t, \\
h_{41} &= \lambda_1 e^{\lambda_1 t}, \\
h_{42} &= \lambda_2 e^{\lambda_2 t}, \\
h_{43} &= \eta_1 e^{\eta_1 t} \cos \omega_1 t - \omega_1 e^{\eta_1 t} \sin \omega_1 t, \\
h_{44} &= \eta_1 e^{\eta_1 t} \sin \omega_1 t + \omega_1 e^{\eta_1 t} \cos \omega_1 t, \\
h_{45} &= \eta_2 e^{\eta_2 t} \bar{k}_5 \cos \omega_2 t - \omega_2 e^{\eta_2 t} \bar{k}_5 \sin \omega_2 t + \eta_2 e^{\eta_2 t} \bar{k}_6 \sin \omega_2 t + \omega_2 e^{\eta_2 t} \bar{k}_6 \cos \omega_2 t, \\
h_{46} &= \eta_2 e^{\eta_2 t} \bar{k}_5 \sin \omega_2 t + \omega_2 e^{\eta_2 t} \bar{k}_5 \cos \omega_2 t - \eta_2 e^{\eta_2 t} \bar{k}_6 \cos \omega_2 t + \omega_2 e^{\eta_2 t} \bar{k}_6 \sin \omega_2 t, \\
\\
h_{51} &= k_1 \lambda_1 e^{\lambda_1 t}, \\
h_{52} &= \lambda_2 k_2 e^{\lambda_2 t}, \\
h_{53} &= \eta_1 e^{\eta_1 t} k_3 \cos \omega_1 t - \omega_1 e^{\eta_1 t} k_3 \sin \omega_1 t + \eta_1 e^{\eta_1 t} k_4 \sin \omega_1 t + \omega_1 e^{\eta_1 t} k_4 \cos \omega_1 t, \\
h_{54} &= \eta_1 e^{\eta_1 t} k_3 \sin \omega_1 t + \omega_1 e^{\eta_1 t} k_3 \cos \omega_1 t - \eta_1 e^{\eta_1 t} k_4 \cos \omega_1 t + \omega_1 e^{\eta_1 t} k_4 \sin \omega_1 t, \\
h_{55} &= \eta_2 e^{\eta_2 t} k_5 \cos \omega_2 t - \omega_2 e^{\eta_2 t} k_5 \sin \omega_2 t + \eta_2 e^{\eta_2 t} k_6 \sin \omega_2 t + \omega_2 e^{\eta_2 t} k_6 \cos \omega_2 t, \\
h_{56} &= \eta_2 e^{\eta_2 t} k_5 \sin \omega_2 t + \omega_2 e^{\eta_2 t} k_5 \cos \omega_2 t - \eta_2 e^{\eta_2 t} k_6 \cos \omega_2 t + \omega_2 e^{\eta_2 t} k_6 \sin \omega_2 t, \\
h_{61} &= \bar{k}_1 \lambda_1 e^{\lambda_1 t}, \\
h_{62} &= \bar{k}_2 \lambda_2 e^{\lambda_2 t}, \\
h_{63} &= \eta_1 e^{\eta_1 t} \bar{k}_3 \cos \omega_1 t - \omega_1 e^{\eta_1 t} \bar{k}_3 \sin \omega_1 t + \eta_1 e^{\eta_1 t} \bar{k}_4 \sin \omega_1 t + \omega_1 e^{\eta_1 t} \bar{k}_4 \cos \omega_1 t, \\
h_{64} &= \eta_1 e^{\eta_1 t} \bar{k}_3 \sin \omega_1 t + \omega_1 e^{\eta_1 t} \bar{k}_3 \cos \omega_1 t - \eta_1 e^{\eta_1 t} \bar{k}_4 \cos \omega_1 t + \omega_1 e^{\eta_1 t} \bar{k}_4 \sin \omega_1 t, \\
h_{65} &= \eta_2 e^{\eta_2 t} \cos \omega_2 t - \omega_2 e^{\eta_2 t} \sin \omega_2 t, \\
h_{66} &= \eta_2 e^{\eta_2 t} \sin \omega_2 t + \omega_2 e^{\eta_2 t} \cos \omega_2 t.
\end{aligned}$$

Note that $h_{41}, h_{41}, \dots, h_{66}$ are the time derivatives of $h_{11}, h_{11}, \dots, h_{36}$, respectively.

Acknowledgments

D.X. thanks the support of the Chinese Scholarship Council. G.G. thanks the Catalan grant government for the grant 2017SGR-1374, and MINECO-FEDER for the grant MTM2016-80117-P. J.J.M. thanks MINECO-FEDER for the grant MTM2015-65715-P and the Catalan government for the grant 2017SGR-1049.

References

- [1] G. Gómez, J. Llibre, and J. J. Masdemont, “Homoclinic and heteroclinic solutions in the restricted three-body problem,” *Celestial Mechanics*, vol. 44, no. 3, pp. 239–259, 1988.
- [2] G. Gómez, W. S. Koon, M. W. Lo, J. E. Marsden, J. J. Masdemont, and S. D. Ross, “Connecting orbits and invariant manifolds in the spatial restricted three-body problem,” *Nonlinearity*, vol. 17, no. 5, p. 1571, 2004.
- [3] E. Canalias and J. J. Masdemont, “Homoclinic and heteroclinic transfer trajectories between Lyapunov orbits in the Sun-Earth and Earth-Moon systems,” *Discrete Contin. Dyn. Syst.*, vol. 14, pp. 261–279, 2006.
- [4] M. Tantardini, E. Fantino, Y. Ren, P. Pergola, G. Gómez, and J. J. Masdemont, “Spacecraft trajectories to the L_3 point of the Sun-Earth three-body problem,” *Celestial Mechanics and Dynamical Astronomy*, vol. 108, no. 3, pp. 215–232, 2010.
- [5] S. Soldini, J. J. Masdemont, and G. Gómez, “Dynamics of solar radiation pressure–assisted maneuvers between Lissajous orbits,” *Journal of Guidance, Control, and Dynamics*, vol. 42, no. 4, pp. 769–793, 2018.
- [6] C. R. McInnes, “Solar sailing: Technology, dynamics and mission control,” *Journal of Guidance Control and Dynamics*, vol. 23, no. 4, pp. 768–768, 2004.
- [7] M. Ceriotti, “Natural and sail-displaced doubly-symmetric Lagrange point orbits for polar coverage,” *Celestial Mechanics and Dynamical Astronomy*, vol. 114, no. 1-2, pp. 151–180, 2012.
- [8] M. Ceriotti, J. Heiligers, and C. R. McInnes, “Trajectory and spacecraft design for a pole-sitter mission,” *Journal of Spacecraft and Rockets*, vol. 51, no. 1, pp. 311–326, 2014.
- [9] M. Walmsley, J. Heiligers, M. Ceriotti, and C. McInnes, “Optimal trajectories for planetary pole-sitter missions,” *Journal of Guidance, Control, and Dynamics*, pp. 2461–2468, 2016.
- [10] G. G. Wawrzyniak and K. C. Howell, “Investigating the design space for solar sail trajectories in the Earth-Moon system,” *The Open Aerospace Engineering Journal*, vol. 4, no. 1, pp. 26–44, 2011.
- [11] J. Heiligers, M. Mac Donald, and J. S. Parker, “Extension of Earth-Moon libration point orbits with solar sail propulsion,” *Astrophysics and Space Science*, vol. 361, no. 7, p. 241, 2016.
- [12] R. J. McKay, M. Macdonald, J. Biggs, and C. McInnes, “Survey of highly non-Keplerian orbits with low-thrust propulsion,” *Journal of Guidance Control and Dynamics*, vol. 34, no. 3, pp. 645–666, 2011.
- [13] C. Gao, W. Wang, J. Yuan, and L. Guo, “Hybrid sail displaced orbits around L_2 point in the elliptic Earth-Moon system,” *Journal of Guidance, Control, and Dynamics*, vol. 42, no. 2, pp. 416–424, 2018.
- [14] S. Soldini, C. Colombo, and S. J. Walker, “Solar radiation pressure Hamiltonian feedback control for unstable libration-point orbits,” *Journal of Guidance, Control, and Dynamics*, vol. 40, no. 6, pp. 1374–1389, 2017.
- [15] J. Heiligers and D. J. Scheeres, “Solar-sail orbital motion about asteroids and binary asteroid systems,” *Journal of Guidance, Control, and Dynamics*, vol. 41, no. 9, pp. 1947–1962, 2018.
- [16] V. Szebehely, *Theory of orbits*. Academic Press, 1967.
- [17] A. Farrés and À. Jorba, “Artificial equilibria in the RTBP for a solar sail and applications,” in *Astrodynamic Network AstroNet-II*, pp. 73–89, Springer, 2016.
- [18] Y. Lian, G. Gómez, J. J. Masdemont, and G. Tang, “A note on the dynamics around the Lagrange collinear points of the Earth-Moon system in a complete Solar System model,” *Celestial Mechanics and Dynamical Astronomy*, vol. 115, no. 2, pp. 185–211, 2013.

- [19] E. M. Alessi, G. Gómez, and J. J. Masdemont, “Further advances on low-energy lunar impact dynamics,” *Communications in Nonlinear Science and Numerical Simulation*, vol. 17, no. 2, pp. 854–866, 2012.
- [20] H. Baoyin and C. R. McInnes, “Solar sail halo orbits at the sun–earth artificial L_1 point,” *Celestial Mechanics and Dynamical Astronomy*, vol. 94, no. 2, pp. 155–171, 2006.
- [21] A. Farrés and À. Jorba, “Periodic and quasi-periodic motions of a solar sail close to SL_1 in the earth–sun system,” *Celestial Mechanics and Dynamical Astronomy*, vol. 107, no. 1-2, pp. 233–253, 2010.
- [22] P. Verrier, T. Waters, and J. Sieber, “Evolution of the halo family in the radial solar sail circular restricted three-body problem,” *Celestial Mechanics and Dynamical Astronomy*, vol. 120, no. 4, pp. 373–400, 2014.
- [23] L. Liu, Y. Liu, J. Cao, S. Hu, G. Tang, and J. Xie, “CHANG’E-2 lunar escape maneuvers to the Sun-Earth L_2 libration point mission,” *Acta Astronautica*, vol. 93, pp. 390–399, 2014.
- [24] H. Peng, X. Bai, J. J. Masdemont, G. Gómez, and S. Xu, “Libration transfer design using patched elliptic three-body models and graphics processing units,” *Journal of Guidance, Control, and Dynamics*, vol. 40, no. 12, pp. 3155–3166, 2017.
- [25] Y. Cheng, G. Gómez, J. J. Masdemont, and J. Yuan, “Study of the transfer between libration point orbits and lunar orbits in Earth-Moon system,” *Celestial Mechanics and Dynamical Astronomy*, vol. 128, no. 4, pp. 409–433, 2017.
- [26] E. Canalias, J. Cobos, and J. J. Masdemont, “Impulsive transfers between Lissajous libration point orbits,” *Journal of the Astronautical Sciences*, vol. 51, no. 4, pp. 361–390, 2003.
- [27] G. Gómez, J. Masdemont, and J. Mondelo, “Libration point orbits: a survey from the dynamical point of view,” in *Libration Point Orbits and Applications*, pp. 311–372, World Scientific, 2003.
- [28] B. Bonnard and M. Chyba, *Recent Advances in Celestial and Space Mechanics*, vol. 23. Springer, 2016.
- [29] A. Delshams, J. J. Masdemont, and P. Roldán, “Computing the scattering map in the spatial Hill’s problem,” *Discrete Contin. Dyn. Syst. Ser. B*, vol. 10, no. 2-3, pp. 455–483, 2008.
- [30] L. Arona and J. J. Masdemont, “Computation of heteroclinic orbits between normally hyperbolic invariant 3-spheres foliated by 2-dimensional invariant tori in Hill’s problem,” *Discrete Contin. Dynam. Systems Suppl*, pp. 64–74, 2007.